THE PENNSYLVANIA STATE UNIVERSITY
SCHREYER HONORS COLLEGE

DEPARTMENT OF CHEMICAL ENGINEERING

Effects of Electronegative Substituents on the Redox Properties of Iron-Salen Derivative Catalysts

BRANDON PERDUE
SPRING 2022

A thesis
submitted in partial fulfillment
of the requirements
for a baccalaureate degree
in Chemical Engineering
with honors in Chemical Engineering

Reviewed and approved* by the following:

Michael Janik
Associate Department Head and Professor of Chemical Engineering
Thesis Supervisor

Darrell Velegol
Distinguished Professor of Chemical Engineering
Honors Adviser

* Electronic approvals are on file.

ABSTRACT

Molecular electrocatalyst performance can be tuned by subtle changes in the electronic structure about the metal active center in order to generate high activity for electrolysis applications. Electrocatalyst performance is highly pertinent for energy, health, and sustainable processes, and therefore rationale modification of supporting ligands can impact important applications. Herein, 12 iron-salen derivatives are examined to determine how the ligand substituents affect redox properties and overall catalyst effectiveness. Density functional theory (DFT) calculations are used to examine the molecular redox reaction energetics. The addition of nitro group ligand substitutions decreases the stabilization of the reduced species formed via an electron-proton transfer. The addition of electron withdrawing groups such as nitro functional groups at multiple ligand positions stabilizes delocalization of charge across the molecule upon reduction. Overall, the study of ligand substituents can greatly impact the field of electrochemical reaction mechanisms and the design of future catalysts.

TABLE OF CONTENTS

LIST OF FIGURES

LIST OF TABLES

ACKNOWLEDGEMENTS

I acknowledge support from the Penn State Chemical Engineering Department in regards to both research and providing me the opportunities to grow as an individual. I would like to particularly thank Dr. Mike Janik for always giving up valuable time to progress my research and my life aspirations. I also thank Dr. Darrell Velegol for always guiding me in the right direction and teaching me valuable life lessons that I will always remember. Furthermore, I acknowledge Joshua Miller for helping me with research over the past three years and working with me through all the challenging times as undergraduates. Finally, I would like to thank Andrew Wong for always being able to help when I was in need of research assistance.

Chapter 1

Introduction

The function of a molecular catalyst is modified by the supporting ligands of a transition metal complex with electron-withdrawing or -donating substituents, such that the inductive effects of the catalyst can be tuned for redox reactions.[1] Therefore, there is a major challenge in catalyst optimization to generate a high activity resulting in, for electrolysis applications, a low overpotential and high electrical energy use efficiency.

The performance of a catalyst is essential for extremely important processes that have revolutionized the fields of energy, health, and sustainability. For instance, redox polymers containing transition metals have attracted interest from researchers due to their wide range of applications, including electronic materials such as catalysis, sensors, memories, solar cells, nanocomposites, energy storage and luminescence materials.[2] Metal complexes with salen ligands, including an anchoring free amine functional group, sustainably reduce CO_2 to alcohols.[3] CO_2 is especially prominent from fossil fuel extraction, and leads to detrimental greenhouse gas effects seen on Earth over the past centuries, motivating scientists to find ways to create valued products and fuels from CO_2.[3] The design of a highly specific-ligand catalyst can create an efficient electrocatalytic mechanism for the conversion of CO_2 into methane, ethanol, and methanol to remove carbon emissions and transition towards cleaner conversion practices whilst producing renewable energy sources.

Molecular Fe-complexes have found applications as electrocatalysts beyond CO_2 reduction. Electrochemical use of carbon-supported iron complexes has also been utilized to

reduce nitric oxide (NO) to hydroxylamine (NH_2OH) for both chemical production and cogeneration of electricity as a fuel cell.[4] This method of coupling the production of a useful chemical with cogeneration of electricity is an extremely attractive and sustainable alternative to conventional chemical processes. Finally, there has been intensive research into developing effective H_2 evolution catalysts for proton exchange membrane fuel cells to produce sustainable energy sources with zero carbon emissions. The use of iron, nickel, and cobalt complexes have been used to develop artificial photosynthesis to make solar energy which provides clean and renewable alternatives for fuel cells.[5] Furthermore, the use of transition metal salen complexes have shown more promise compared to that of platinum due to high costs of noble metals and scarcity which cause limitations to its widespread use. According to the salen ligand research, the coordination sites and ancillary ligands have been found to control the catalytic transformations of the hydrogen production and stabilize the various oxidation states, showing the versatility of the ligands of salen complexes.[5] Catalysts that utilize Co-salen complexes have been found to synthesize linear and branched benzylic, heterocyclic and aliphatic primary amines from carbonyl compounds and ammonia, which are essential for life and material sciences such as drugs and Nylon-6. Therefore, the specificity of the catalyst is important for advanced organic synthesis that are highly impactful for the future of the pharmaceutical industry.

Nitrobenzene (NB) is highly toxic to aquatic life, and hence needs removal from water sources at high concentrations.[6] NB can be reduced through thermal hydrogenation or electrocatalytic reduction. NB can be reduced to aniline, an important chemical and intermediate in the production of pharmaceuticals, dyes, pigments, and pesticides, using highly functional transition metal catalysts.[7] Overall, the functionalities of these compounds are essential to their effectiveness and activity. There are many advantages to the use of electrocatalysis compared to

biological and chemical use. For instance, the use of an electrode is cost-effective and environmentally sustainable since the electrons are supplied throughout the reaction. Additionally, the reaction conditions are performed under typical operating conditions and can easily be manipulated to create a high selectivity towards the target product.

Overall, the use of salen complexes as molecular catalysts, specifically, have shown transformative possibilities in a multitude of fields, making them a valuable field of study. In this study, 12 iron-salen derivatives were examined to determine the effectiveness of ligand substituents on their redox properties. Salen derivatives were chosen as they are more easily synthesized, are extremely versatile as discussed previously, and can be manipulated easier for asymmetric active metal site environments.[8] The general structure of each catalyst is shown in **Figure 1**[1], and the derivatives of this experiment follow that of Böttcher's application, as seen in **Figure 2.**[9]

Figure 1. General structure of iron salen complexes studied with modified redox properties via inductive effects at the 'R' substituents[1]

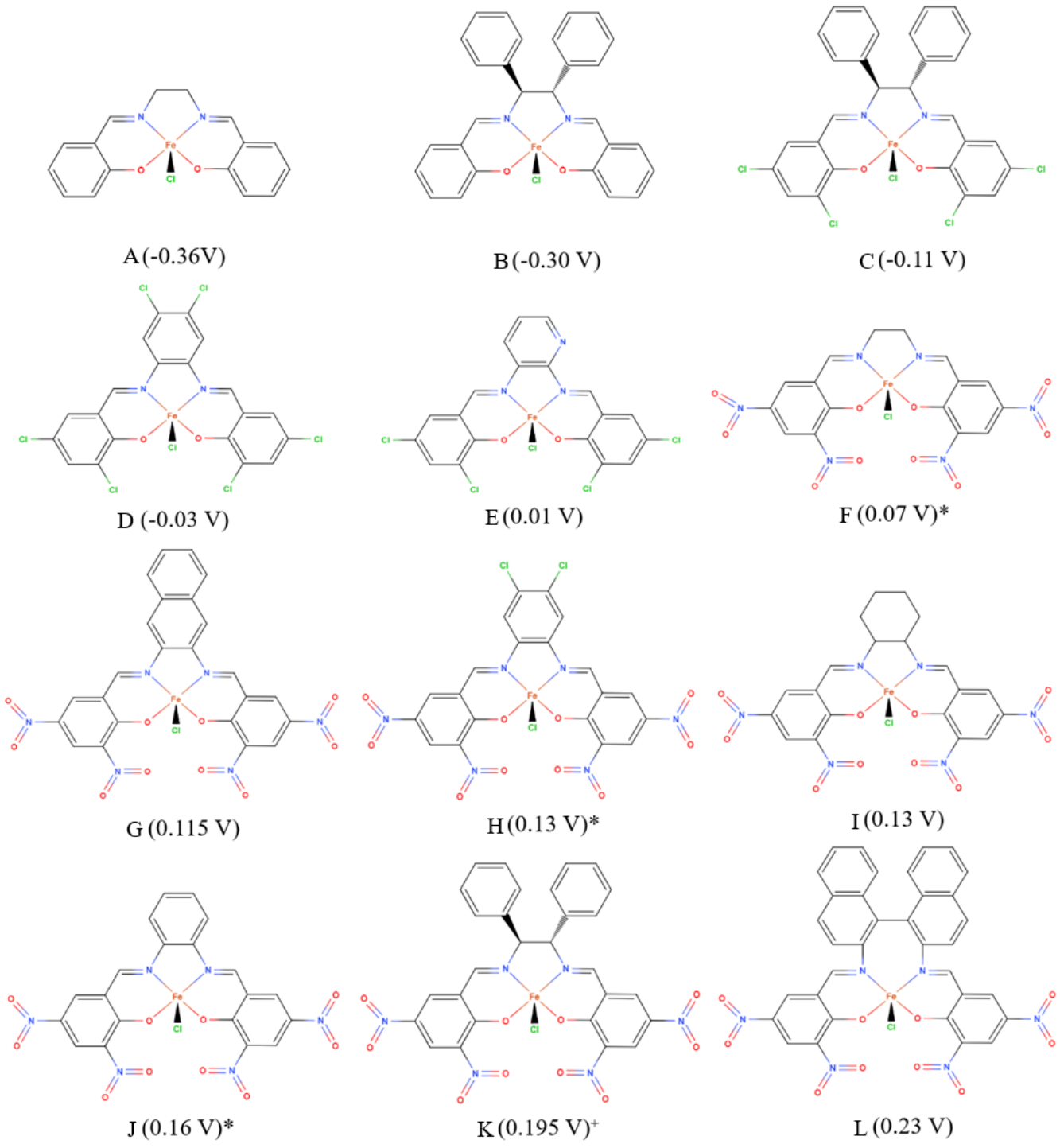

Figure 2. Structures of the electronegative iron salen derivatives studied and their iron (III/II) reduction potentials (V vs. AgCl/Ag) measured in 0.1 M tetra-n-butylammonium tetrafluoroborate/CH_3CN. * In DMF. + In CH_2Cl_2[9]

Böttcher's results shows that the catalytic activity arises from the substitution of halogens which inhibits oxidative destruction of the catalyst, and a lower iron oxidation state stability which permits Fe (III) complexes to oxidize peroxides, which is typically a slow step in peroxide decomposition.[9] In this thesis, the reduction of the 12 catalysts will be analyzed, as the redox potential and mechanism impacts the catalytic activity of the iron organometallic complexes. We consider reduction energetics for electron transfer and coupled electron/proton transfer, elucidating the stable redox state of the catalyst as a function of operating potential and pH. Using density functional theory (DFT), the calculations provide redox energetics that dictate the electrocatalytic reduction of compounds. DFT will be utilized to connect the functionalities of each complex's ligand substitutions to their redox potentials to ultimately determine the effect on catalytic activity.

Chapter 2

Methods

2.1 Electronic Structure Methods

Density functional theory (DFT) was utilized to analyze the structure of intermediate and transition state catalysts during the reduction pathway for all 12 Fe-salen complexes. The Vienna ab initio simulation package (VASP) was used to perform all DFT calculations, employing a plane wave-basis set and the projector-augmented wave (PAW) approach to include the interactions of core-valence electrons.[10-12] The Perdew, Burke, and Ernzerhof (PBE) generalized gradient approximation (GGA) calculated the exchange and correlation energies.[13,14] A 7 x 7 x 1 Monkhorst pack grid was used to sample *k*-space for surfaces.[15,16] The cutoff energy value for the plane-wave basis set was set at 450 eV. The convergence of the self-consistent electron density was set at 10^{-5} eV. The structural optimizations were complete when the forces on all atoms were less than 0.02 eV $Å^{-1}$. Unrestricted spin calculations were performed for all catalytic optimizations. Initial structures of each molecular catalyst were built using Amsterdam Modeling Suite (AMS) in a 25 Å periodic cubic unit cell. DFT and statistical mechanics were utilized to study the thermodynamics of catalyst reduction. The free energies of reduction of the catalysts were calculated as a function of potential. Equilibrium potentials, which represent the potential where formation of a certain reduction state of the catalyst is favorable, was determined.

2.2 Calculation of Potential Dependent Reaction Free Energies

The reduction pathway analyzed for each catalyst (Cat) species is

$$Cat + e^- \rightarrow Cat^- \quad (1)$$

$$Cat + H^+ + e^- \rightarrow CatH \quad (2)$$

$$CatH + e^- \rightarrow CatH^- \quad (3)$$

$$CatH + H^+ + e^- \rightarrow CatH_2 \quad (4)$$

The Gibbs free energy change of the reduction reaction to form a given species or intermediate *i* represented as products above from (1) to (4), ΔG_{red}, is denoted

$$\Delta G_{red} = G_i - G_{cat} - nG_{H^+ + e^-} + mG_{e^-} \quad (5)$$

where *n* is the number of coupled proton-electron pairs transferred (*n*→0,1,2) and *m* represents the total number of uncoupled electrons transferred (*m*→-1,0,1). A cation reduced intermediate is represented with an *m* value of -1, while an anion reduced intermediate species is represented with an *m* value of 1. G_i, G_{cat}, $G_{H^+ + e^-}$, and G_{e^-} represent the Gibbs free energy of the catalyst, intermediate/product analyzed, proton-electron pair, and electron, respectively.

The computational hydrogen electron approach was utilized in (5) to model the free energies of both a proton and electron.[17] The following method for computational hydrogen electrode defines the chemical potential of a proton-electron pair as the chemical potential of half

a hydrogen molecule at 0 V on an RHE scale. This linearly corrects the addition of an electron's energy to a reference electrode. The following is shown in (6), and is denoted as $G_{H^+ + e^-}$

$$G_{H^+ + e^-} = \frac{1}{2} G_{H_2} - |e^-| U_{RHE} \tag{6}$$

where G_{H_2} represents the free energy of molecular hydrogen, e^- denotes the charge of an electron, and U_{RHE} represents the electrode potential relative to the RHE scale.

The contribution of uncoupled proton-electron transfer during the inner-sphere mechanism to the free energy model of equation (5) is denoted as G_{e^-}. In this model, the electron and its Gibbs free energy is dependent on the potential of the applied electron on a normal hydrogen electrode (NHE) reference

$$G_{e^-}(U_{NHE}) = -|e^-| U_{NHE} - |e^-| \Delta U_{abs} \tag{7}$$

where ΔU_{abs} is the absolute potential of the NHE scale. This study used a value for ΔU_{abs} (NHE) equal to 4.6 V, which is commonly used for comparisons for similar DFT calculations on nitroaromatics reduction pathways.[18] Combining (6) and (7) into equation (5) yields an overall equation (8)

$$\Delta G_{red} = G_i - G_{cat} - \frac{n}{2} G_{H_2} + n|e^-| U_{NHE} + m|e^-|(U_{NHE} + \Delta U_{abs}) \tag{8}$$

Therefore, equation (8) calculates the potential dependent free energy to form a reduction intermediate or product based on an NHE scale, relative to the reactant, or initiating species. This forms the reaction free energy diagram at pH of 0.

2.3 Pourbaix Diagram Construction and pH Species Intersection

Pourbaix diagrams were formed to detail the potential (on a NHE scale) and pH ranges at which a given redox state of each catalyst is most stable. The relative free energy of protonated catalytic intermediates dependence on pH were calculated with

$$V - NHE = \Delta G_{red} - 0.0591pH \tag{8}$$

where ΔG_{red} was determined at an initial pH of 0. The pH at which a non-protonated, uncoupled intermediate was determined to intersect the first protonated catalytic intermediate (CatH) is determined as

$$pH = \frac{\Delta G_{Cat^-} - \Delta G_{CatH}}{-0.0591} \tag{9}$$

where ΔG_{Cat^-} and ΔG_{CatH} are the free energies of the unpaired electron and paired proton and electron catalytic intermediate species, respectively. The regions considered were of standard pH range, between 0 and 14.

Chapter 3

Results and Discussion

3.1 Reaction Energy Mechanisms of Catalyst Reduction

Figure 3 depicts the reaction energy diagrams of the electrochemical reduction of both the non-halogenated and halogenated ligand substituent species, or A—E, at 0 V-NHE and 0 pH. The reaction energy diagrams for the nitro group ligand species F—L are compared in **Figure 4**. The two-electron reduction energy for each species is located in **Table 1**, as well as their equilibrium potentials. All DFT results are determined on a relative scale of 0 V-NHE, therefore with a significant reduction overpotential relative to nitroaromatic reduction equilibrium potentials that are greater than 0.5 V-NHE. Individual species reaction energy diagrams are located in **Appendix A**.

Table 1. Reduction energies at 0 V-RHE and equilibrium potentials (on an RHE scale) to reduce iron-salen complexes from X to XH_2. Species labels are given in Figure 2.

Species	Overall Reduction Energy (eV)	Equilibrium Potential (V-RHE)
A	-0.14	0.072
B	0.15	-0.074
C	0.32	-0.159
D	0.70	-0.351
E	0.68	-0.338
F	-0.34	0.169
G	-0.54	0.418
H	-0.56	0.282
I	-0.60	0.299
J	-0.54	0.270
K	-0.62	0.311
L	-1.14	0.568

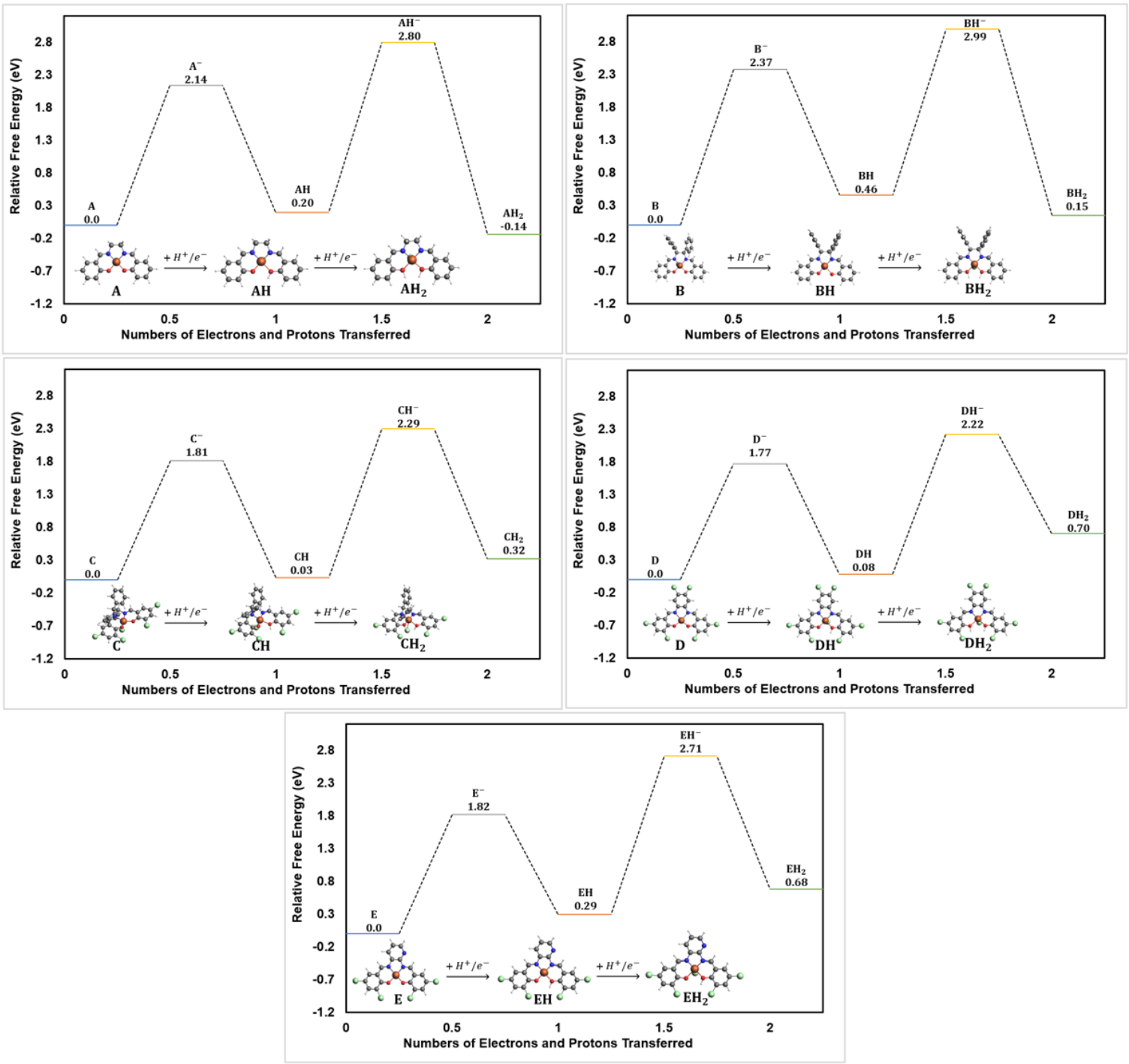

Figure 3. Reaction energy diagrams for electrochemical reduction of catalyst species A through E, calculated using the VASP code and model. Energies are relative to the original catalyst species at 0 V-NHE and 0 pH. Most stable configuration of each reduced intermediate is used. Atom colors are presented by gray: C, white: H, blue: N, and red: O

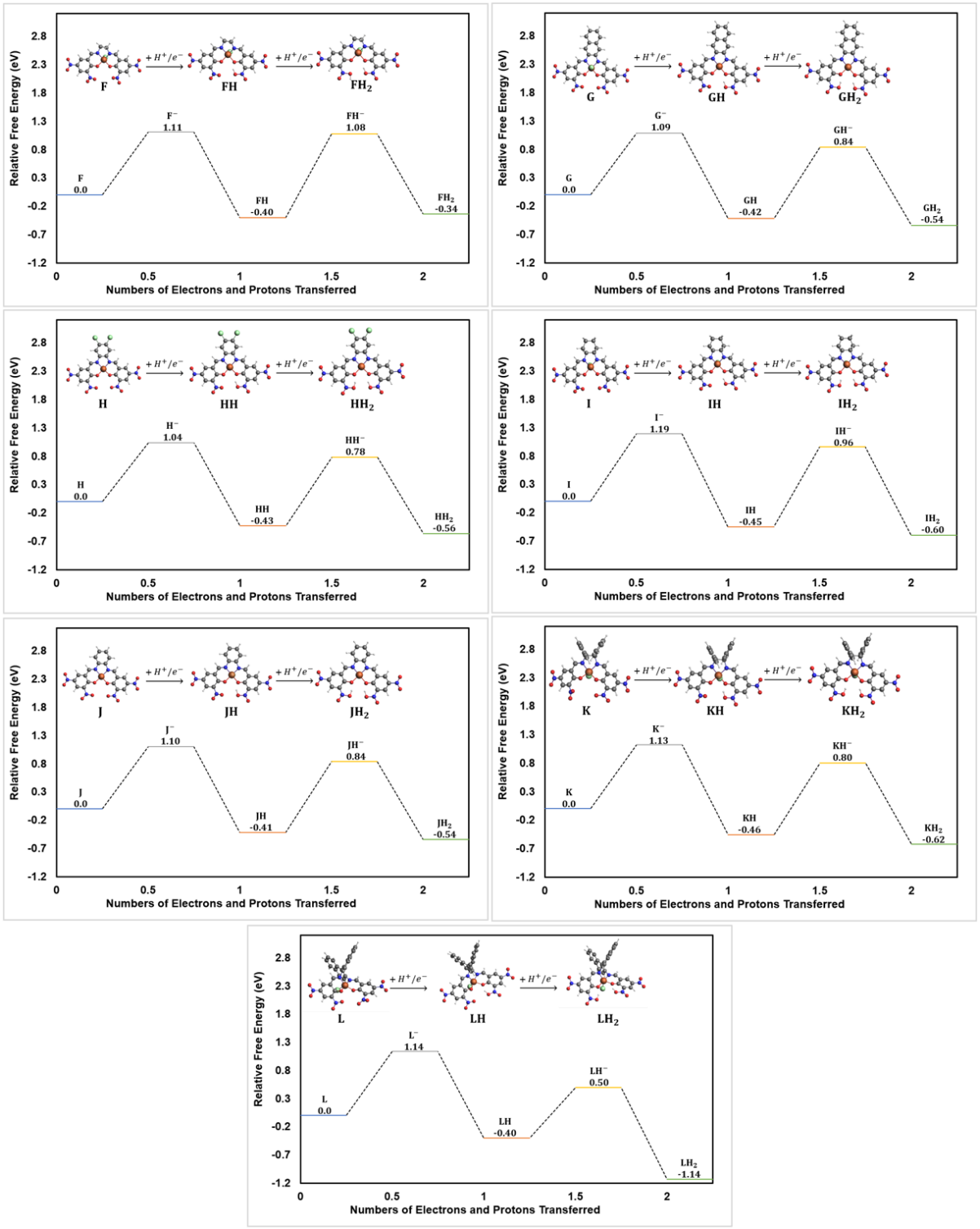

Figure 4. Reaction energy diagrams for electrochemical reduction of catalyst species F through L, calculated using the VASP code and model. Energies are relative to the original catalyst species at 0 V-NHE and 0 pH. Most stable configuration of each reduced intermediate is used. Atom colors are presented by gray: C, white: H, blue: N, and red: O

Figure 3 shows that both catalyst structures A and B have large uphill energies for the uncoupled electron transfer steps. Furthermore, the coupled proton-electron transfer steps are also higher in energy than the original species at 0 V-RHE. Therefore, with no electron withdrawing ligand substituents, the reduction mechanism for the two species is unfavorable at 0 V-RHE. With the addition of chlorine atoms on ligand substituents for catalysts C, D, and E, the large uphill nature of the uncoupled electron transfer steps decreases overall by approximately 0.46 eV at 0-VHE. However, all three catalysts, while possessing more electron withdrawing groups, show an increase in energy for the coupled proton-electron transfer steps relative to the initial species. Consequently, while the addition of chlorine atoms does stabilize both negatively charged species in the mechanism, their effects are still limited on the overall reduction process.

The limitations of chlorine as a stabilization for the reduction mechanism are especially evident when comparing to catalysts F through L in **Figure 4**. Species F through L contain additional nitro groups as ligand substituents, which change the reduction energetics as compared to the previous five catalysts aforementioned. First, there is a more dramatic decrease in uphill energies for the uncoupled electron transfer steps, equating to an average decrease of approximately 1.32 eV. Therefore, the reduction in reaction energy for the first and third steps of the mechanism indicate that the nitro groups as substituents additionally stabilize the introduced electron in the negative species. Consequently, nitro groups act as more favorable functional groups for the reduction pathways in regards to these complexes.

The limiting effects of chlorine substituents are also seen between the transition energies between catalysts G and H. With nearly identical reaction mechanism diagrams, the slight favorability seen in regards to species H indicates that chlorine somewhat stabilizes, but not nearly as effective compared to the changes seen with nitro group ligand substituents.

Nonetheless, the effects are evident, as seen also between the energy favorability of catalyst H relative to catalyst I. Additionally, the fully reduced species for catalysts K and L are significantly less downhill compared to catalysts A—J. Therefore, the addition of conjugated rings as ligand substituents also stabilizes reduction, especially for the final reduced species.

3.2 Catalyst Reduction Equilibrium Potential

The reduction equilibrium potentials for the coupled proton-electron transfer ($X \rightarrow XH$) versus the uncoupled electron transfer ($X \rightarrow X^-$) were compared for each catalyst in **Figure 5**. There is a clear correlation between these two reduction energies, showing the stability of the reduced XH species correlates with that of X^-. Note that the span of reduction potentials to form X^- is over 2 V whereas that of XH is approximately 1 V. This suggests that the variation in ability to stabilize the negative charge in the X^- anion impacts the reduction potential to form the XH intermediate, however, as protonation somewhat localizes the charge, there is less span in stability with variation in substituents for the protonated species.

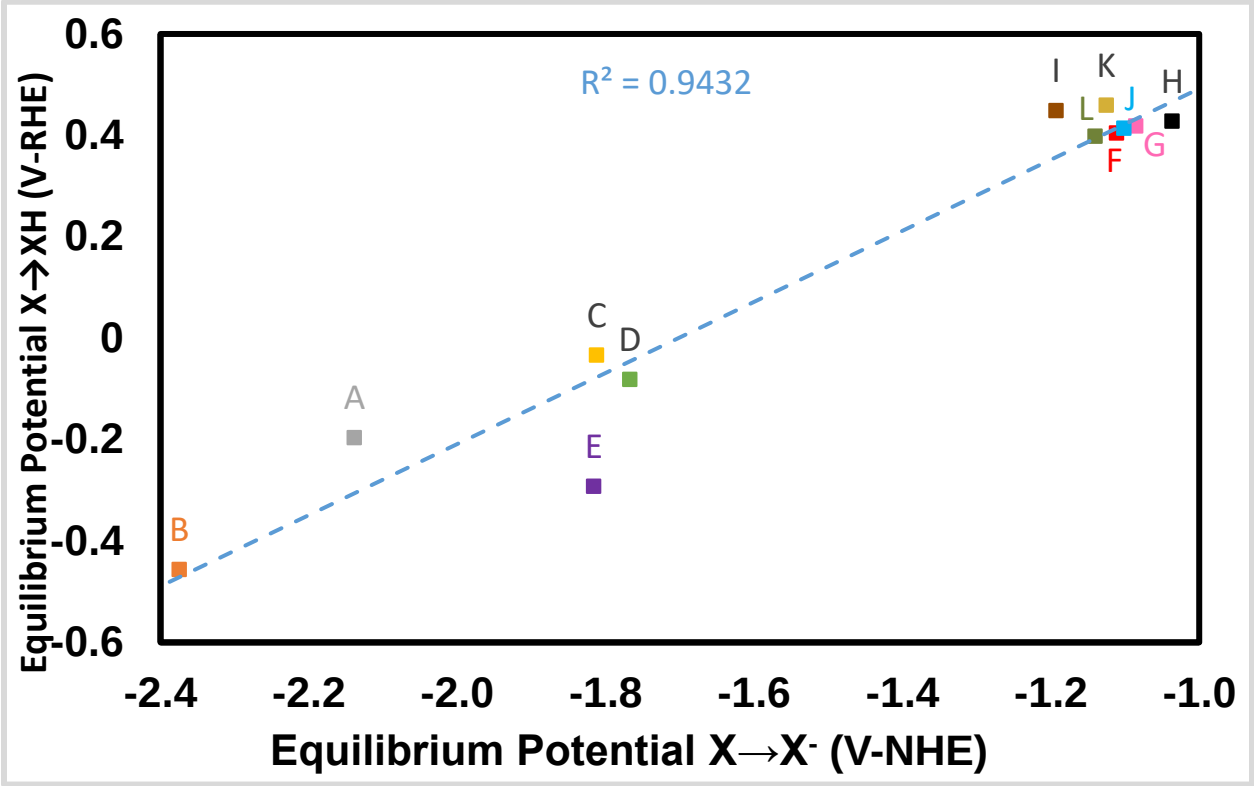

Figure 5. Equilibrium potential of the first coupled proton-electron transfer versus the equilibrium potential of the first uncoupled proton-electron transfer for each catalyst

Figure 5 clearly depicts two distinct regions, with A—E at lower equilibrium potentials and F—L at higher equilibrium potentials for both transfer mechanisms. These regions are clearly representative of the differentiation due to additional electronegative ligand substituents. The trend overall indicates that from catalyst A to L, when the equilibrium potential of the first uncoupled proton-electron transfer ($X \rightarrow X^-$) increases, so does the equilibrium potential for the first coupled proton-electron transfer ($X \rightarrow XH$). Therefore, the reduction capabilities of the species are increasing with additional electron withdrawing groups as ligand substituents.

The equilibrium potential between A—E and F—L for the uncoupled transfer is approximately an increase of 0.6 V-NHE, while the increases of the coupled transfer equate to 0.4 V-RHE. This follows the familiar trends evident in the energy mechanisms in a linear nature.

As seen in the energy mechanisms, there was a large decrease in the reaction energy for the uncoupled electron transfer mechanisms, which is evident with high favorability of the nitro group substituent catalyst species in the top right corner of **Figure 5**. The stability of the coupled proton-electron transfer is also depicted for the nitro group species due to high equilibrium potentials.

Additionally, the effects of chlorine ligand substitution are more evident between B and C/E. The trend indicates an uncoupled transfer increase approximately equal to that seen in the change from chlorine to nitro group ligand substitutions. However, the favorability for the coupled proton-electron transfer was closer to 0.2 V-RHE, which is approximately half of the increase seen from the transition to nitro group catalysts. The use of both chlorine atoms and nitro groups, however, increased the stabilization and favorability of the catalyst species, as depicted by catalyst species H. Catalyst H possesses the most favorable X→X- species, and is the second most favorable X→XH species in regards to equilibrium potential. Therefore, the combined use of chlorine and nitro groups provide an even greater stability for the reduction mechanisms. The only species with a higher equilibrium potential for the coupled proton-electron transfer is catalyst K, as seen by the large downhill energy seen in **Figure 4**.

3.3 Catalyst Reduction Pourbaix Diagrams

The favorability for a given intermediate of the catalysts as a function of V-RHE with a pH = 0 is depicted for catalysts A—E in **Figure 6** and catalysts F—L in **Figure 7**. These figures can also be found individually in **Appendix A**. These figures give the relative energy of species XH and XH_2 relative to X as a function of voltage. The species that are lowest energy at any

given potential are most stable, and coloring is added to the figure to show the different voltage regions at which X, XH, and XH_2 are the most stable species. This figure is generated at one pH, however, the relative stability of XH and XH_2 relative to X does not depend on pH on a RHE scale. The energy to protonate a species (X^- to XH, XH^- to XH_2) is a function of pH. Pourbaix diagrams allow us to combine the impact of voltage on pH on the stability of the various redox states and protonation states of the X species. Pourbaix diagrams were constructed for each species, and catalysts A—E are depicted in **Figure 8**, while **Figure 9** contains Pourbaix diagrams for catalysts F—L. Likewise, Pourbaix diagrams for each species are located in **Appendix A**.

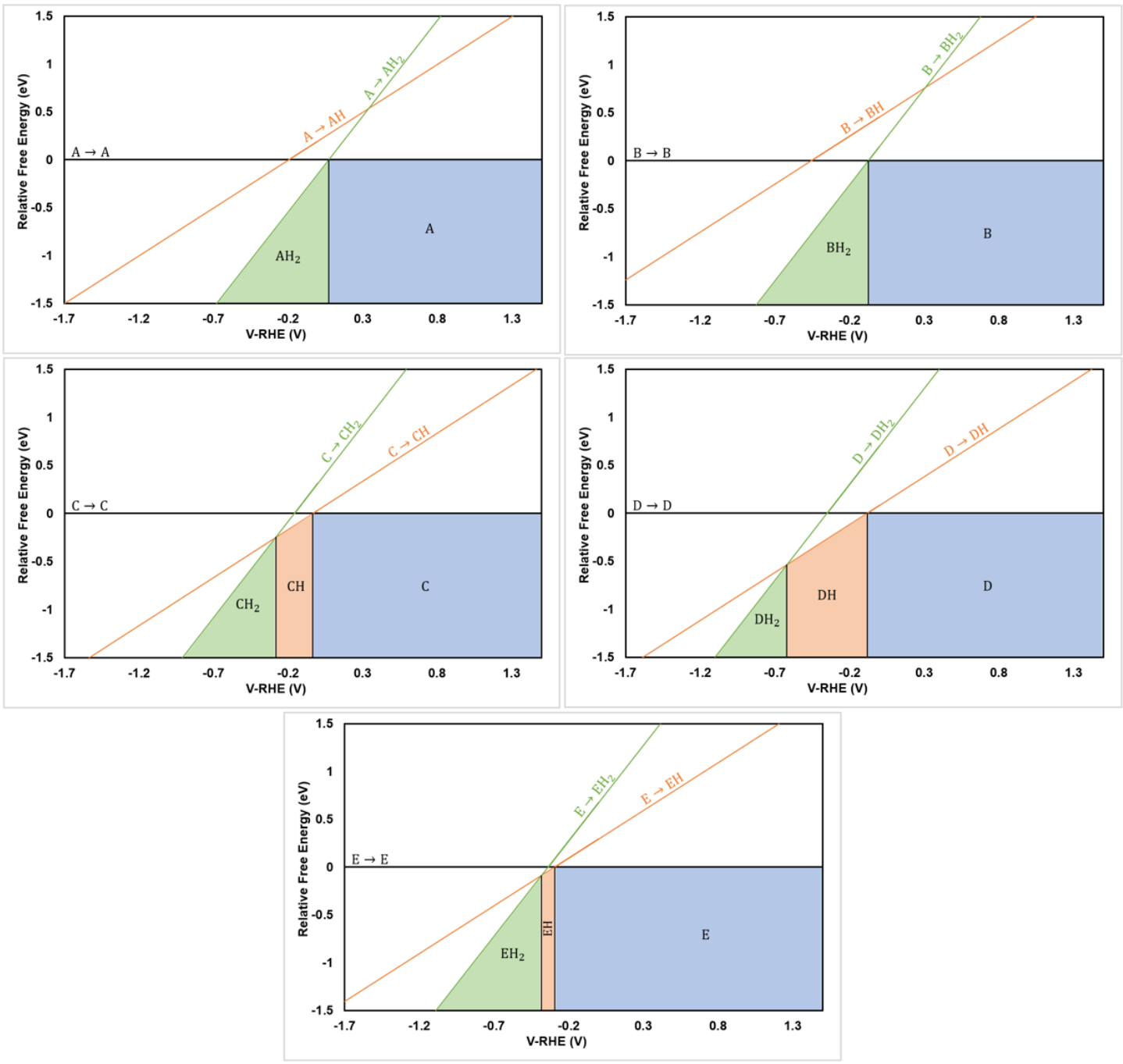

Figure 6. Relative energy potential differences of coupled proton-electron transfers on a V-RHE scale at pH = 0 with favorable species regions for catalysts A through E

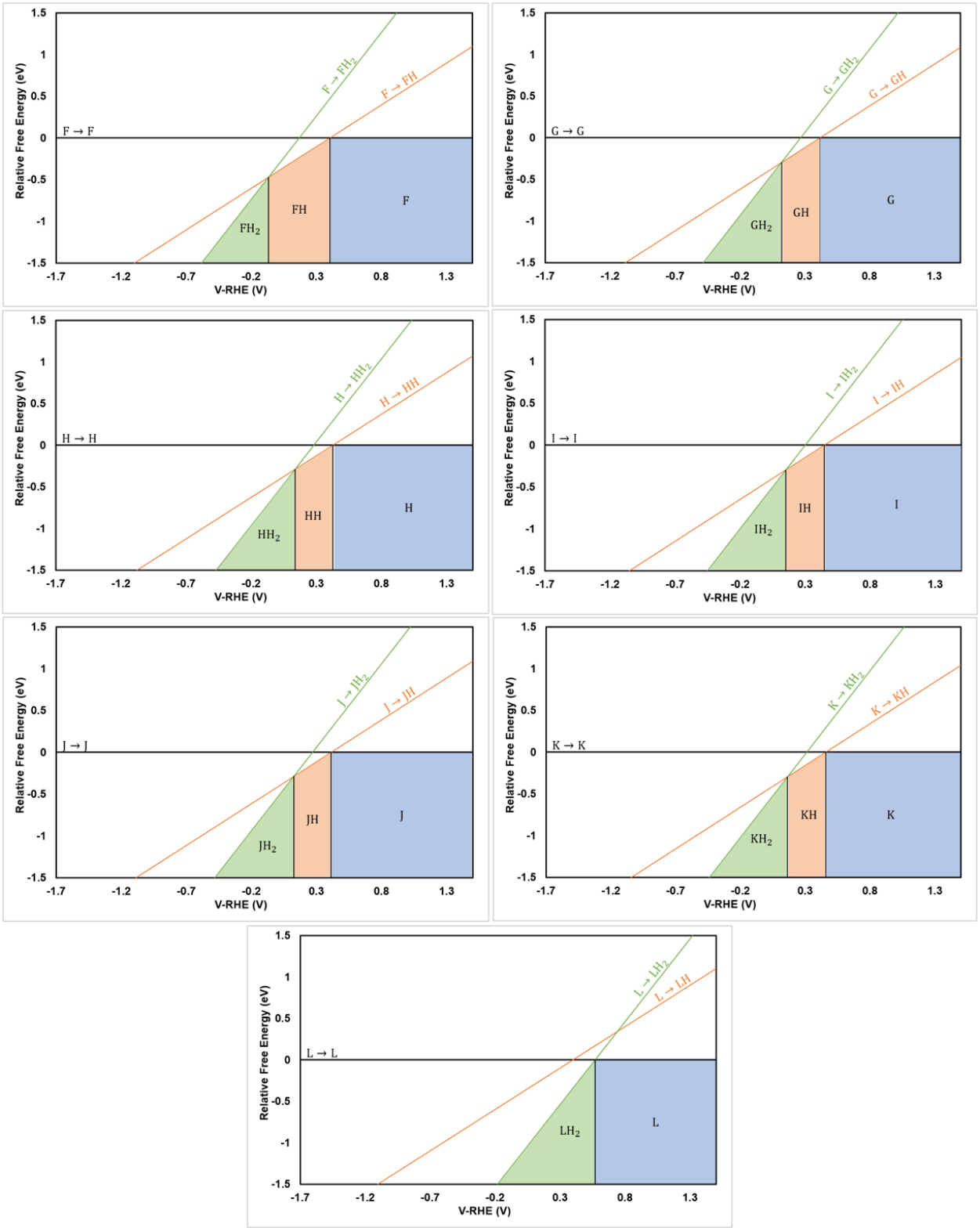

Figure 7. Relative energy potential differences of coupled proton-electron transfers on a V-RHE scale at pH = 0 with favorable species regions for catalysts F through L

From **Figure 6**, there is a clear indication that for catalysts A and B are stable in their initial unreduced forms at a wide range of potentials. Largely negative potentials are needed to induce the reduction of the catalyst to the XH_2 species, therefore making the catalysts with no electron withdrawing groups unfavorable to reduce, and therefore, to act as electron transfer agents within reduction mechanisms. The difficulty to promote reduction is indicated with catalysts C, D, and E. The halogenated substituent ligands create a new XH region in **Figure 6** with transition values closer to zero, indicating more favorability towards reduction mechanisms. However, the transitions are still below zero which evidently still lacks the higher redox potentials needed for reduction at potentials near nitroaromatic reduction equilibrium potentials. However, the introduction of halogenated species to stabilize the reduction indicates an increase in the catalyst's behavior to accept coupled proton-electron transfers. With the introduction of nitro group ligand substituents, there is an evident shift to smaller, initial reactant catalyst regions (X species). The decreased size with the transition to nitro group catalysts of F—L indicates that there are more prominent, stabler reductive catalyst species such as XH and XH_2. **Figure 7** depicts those transitions to XH in F—K are all significantly above 0 V-RHE, which indicates high favorability to reduce these nitro group catalysts. Catalysts F—K also are extremely similar, with little to no variation between catalyst figures with **Figure 7**. Therefore, the effects of increasing the reduction potential are minimal between the six nitro group catalyst species aforementioned.

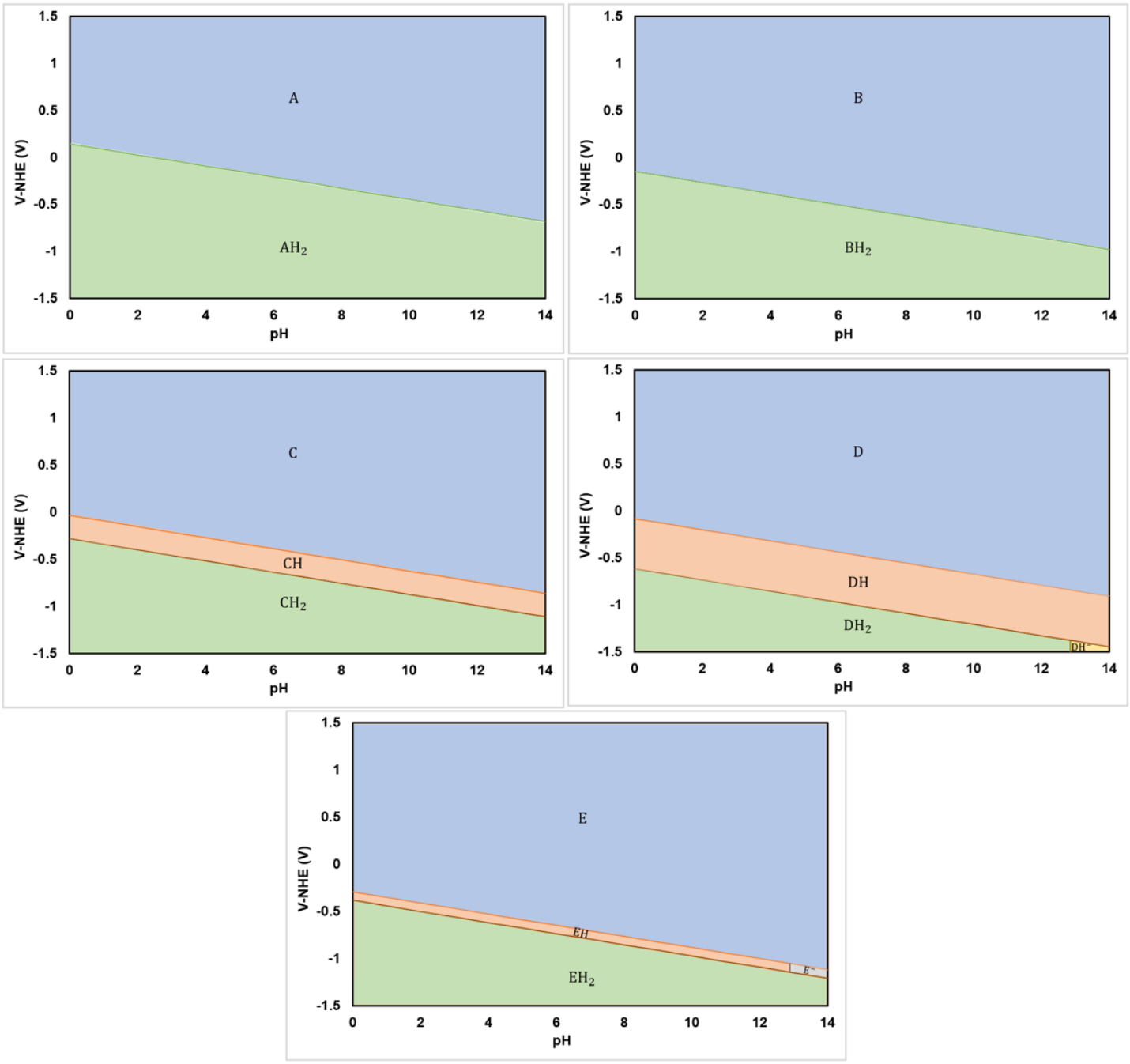

Figure 8. Relative energy potential differences of reaction mechanism steps on a V-NHE scale with favorable species regions versus pH conditions with favorable species regions for catalyst A through E

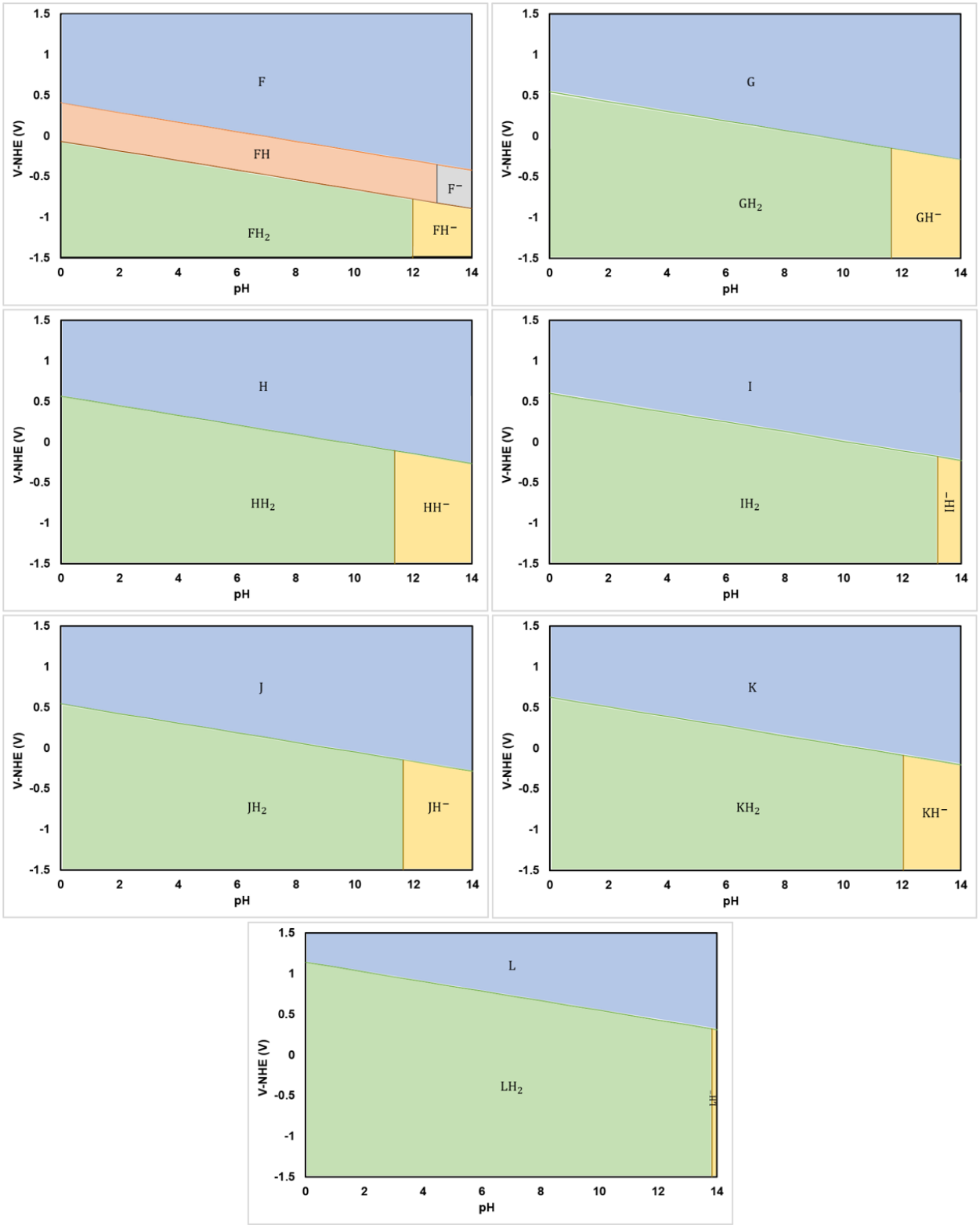

Figure 9. Relative energy potential differences of reaction mechanism steps on a V-NHE scale with favorable species regions versus pH conditions with favorable species regions for catalyst F through L

Figure 8 indicates similar results for A and B as seen from **Figure 6**, with no XH region existing and a transition specifically from $X \rightarrow XH_2$. The region in which the original catalyst species exists in much wider in range than catalysts C—L, once again concluding the limited reduction capabilities without the electron withdrawing ligand substituents. Catalysts C, D, and E also depict similar results to that corresponding to their respective catalyst in **Figure 6**. However, due to the stabilizing capabilities of the electron withdrawing chlorine atoms attached to the ligands, the intermediate species X^- and XH^- become prevalent, indicating that there are small regions in which the reductive catalytic environment has stable intermediates for uncoupled electron transfer.

Additionally, there is a stark difference between the favorable species under the given conditions for catalysts F—L. First, the regions in which the original catalyst X exists drastically decreases in size, indicating that the reduced intermediate catalyst species are more prevalent under the range of conditions considered. The regions in which $X \rightarrow X^-$ and $XH \rightarrow XH^-$ lower in pH such that they decrease to a normal pH regime between 0—14. For catalyst F, there are two larger regions relative to other catalyst Pourbaix diagrams in which X^- and XH^- are stable intermediates, indicating that the nitro additions to the ligands significantly impact the redox potentials. Catalysts G—L act differently from catalyst F, in which the first stable reaction is $X \rightarrow XH_2$. Therefore, overall reduction is quite favorable and there is not potential region in which the first coupled proton-electron transfer species is stable – it is metastable and would further reduce to XH_2 once formed. This full transition also highlights the strong capabilities for the nitro groups to completely stabilize the compound such that the transition to the second

coupled proton-electron transfer is extremely quick and essentially acts as one fast step rather than the having an XH region.

Chapter 4

Summary and Conclusions

DFT methods were used to investigate the effects of electronegative substituents on the thermodynamics of catalytic reactions of 12 iron-salen derivative catalysts. The reaction mechanisms for the reduction of each catalyst from two coupled proton-electron transfers were determined, and showed a clear trend that the electron withdrawing groups had a direct impact on the stability of the coupled proton-electron transfers, as well as increased favorability for the uncoupled electron transfer. Overall, the nitro group ligand substitutions proved greater impact relative to those catalysts that used chlorine substitutions. The trend of equilibrium potential for reactions X→XH versus X→X- resulted in their being a direct, increasing relationship between the two potentials. Therefore, the nitro groups showed a much higher equilibrium potential for both reactions, while the chlorinated and non-electron withdrawing substituted catalysts located at much lower potentials. Pourbaix diagrams yielded similar results, with high basic pH values for nitro groups showing stable X^- and XH^- regions, indicating the stability of the electron within the catalyst complex with additional strong conjugated ligand substitutions.

Limitations in this analysis include using no solvation models for DFT calculations, which neglect many key interactions between molecules and electric field effects. Future work would include testing the effects of solvation modeling to compare the results and trends of both calculations. The effects of electron spin states should also be considered for future work to ensure the most accurate representation of mechanisms and stability regions for each species.

Appendix A

Supporting Information

Table 2. Molecular images and energies for catalyst species X

Species	Image of Lowest Energy State	Energy (eV)
A	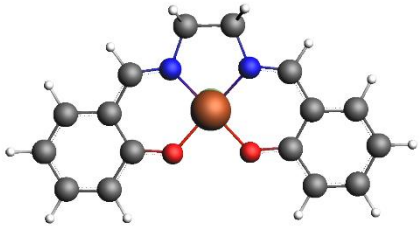	-236.319
B	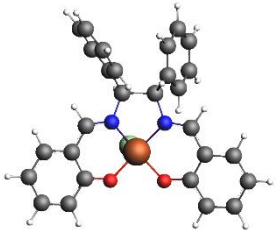	-373.857
C	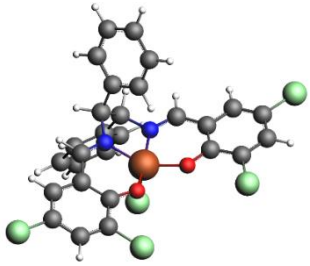	-367.449
D	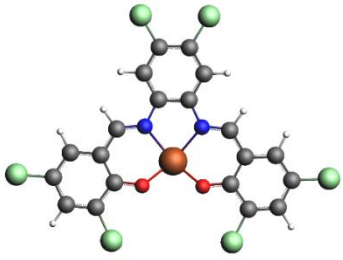	-263.531

E	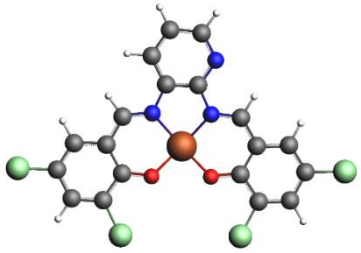	-261.960
F	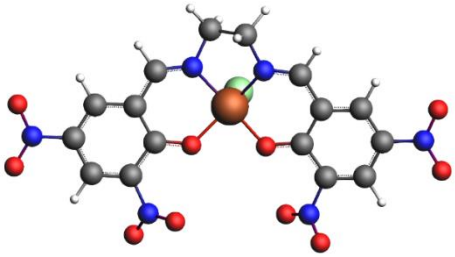	-297.500
G	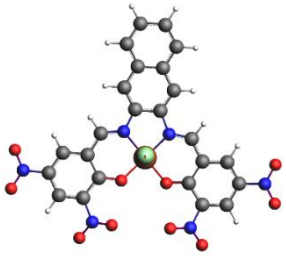	-376.927
H	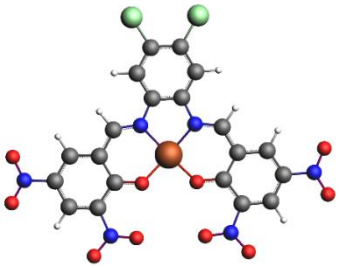	-330.280
I	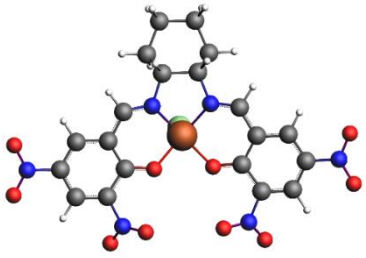	-355.998

J	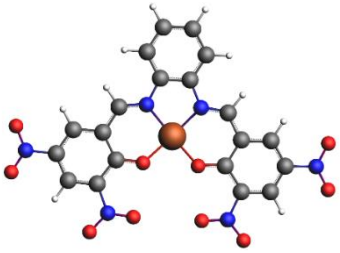	-333.357
K	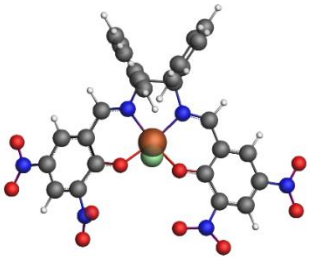	-434.598
L	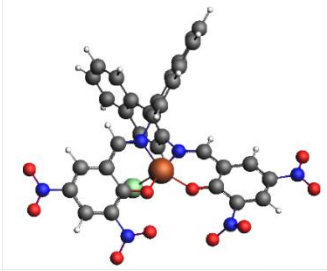	-488.326

Table 3. Molecular images and energies for catalyst species X^-

Species	Image of Lowest Energy State	Energy (eV)
A^-	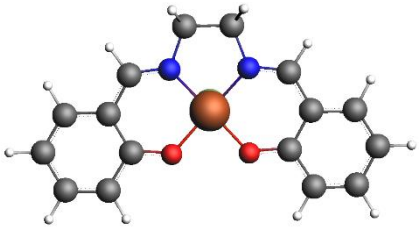	-238.780
B^-	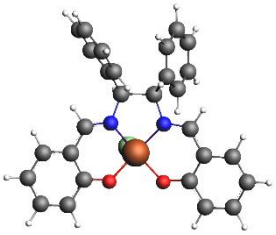	-376.082

C^-	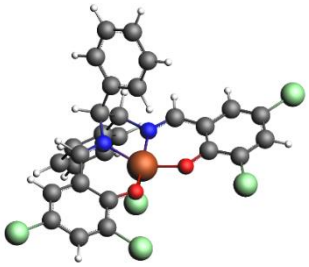	-370.237
D^-	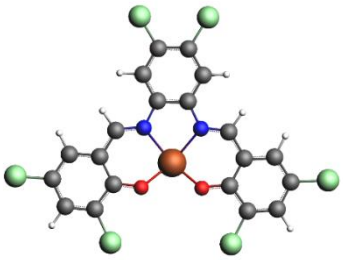	-266.363
E^-	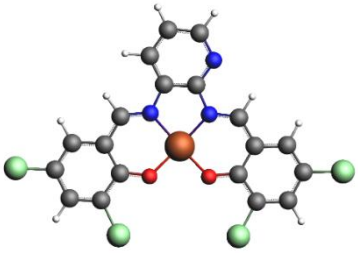	-264.745
F^-	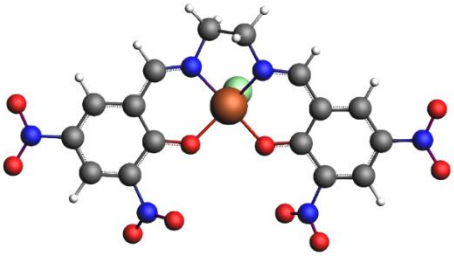	-300.989
G^-	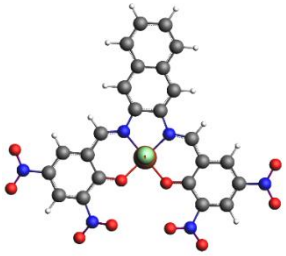	-380.442

H^-	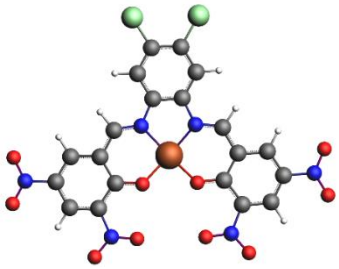	-333.843
I^-	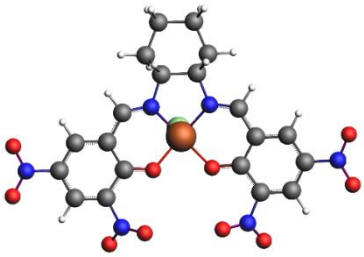	-359.405
J^-	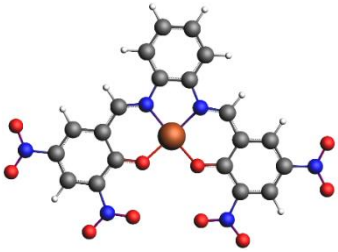	-336.856
K^-	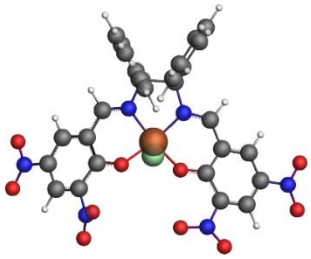	-438.072
L^-	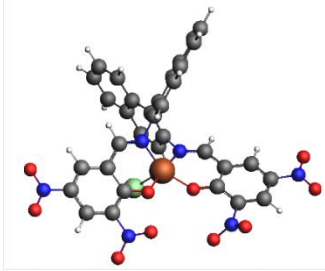	-491.786

Table 4. Molecular images and energies for catalyst species XH

Species	Image of Lowest Energy State	Energy (eV)
AH	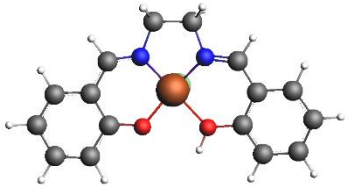	-239.558
BH	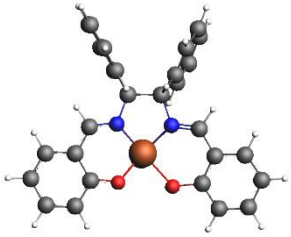	-376.836
CH	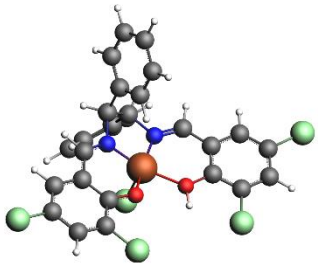	-370.851
DH	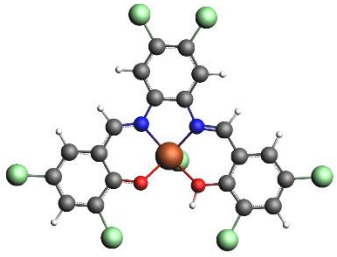	-266.885
EH	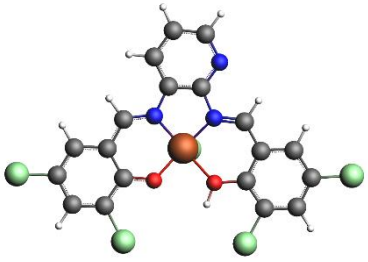	-265.104

FH	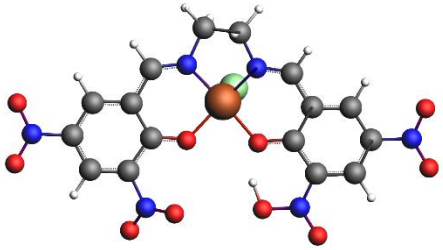	-301.340
GH	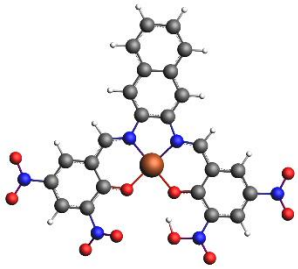	-380.781
HH	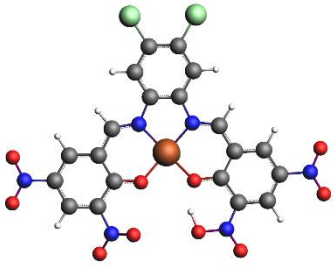	-334.143
IH	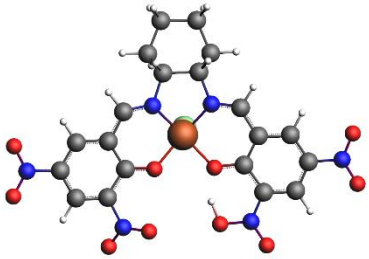	-359.882
JH	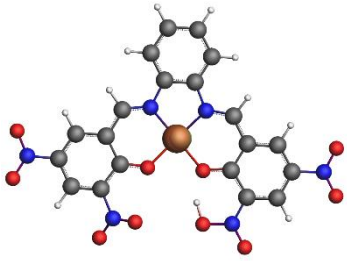	-337.207

KH	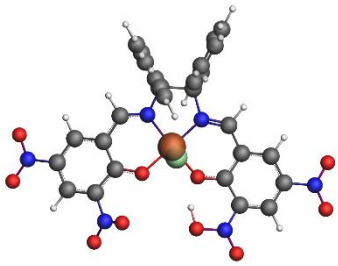	-438.493
LH	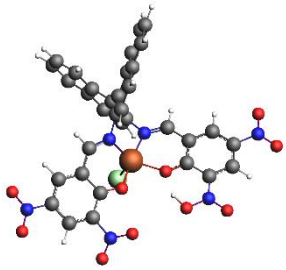	-492.612

Table 5. Molecular images and energies for catalyst species XH^-

Species	Image of Lowest Energy State	Energy (eV)
AH-	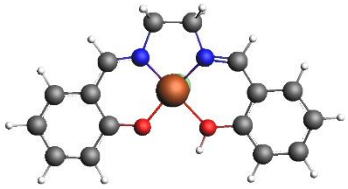	-241.558
BH-	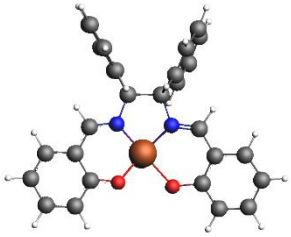	-378.907
CH-	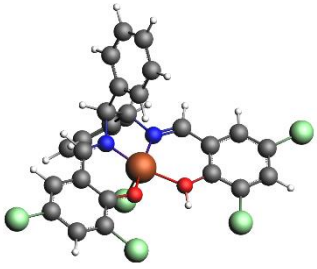	-373.191

DH-	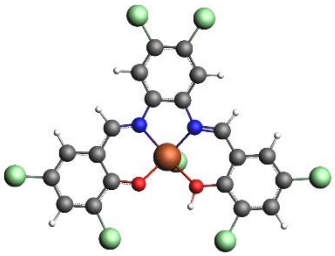	-269.344
EH-	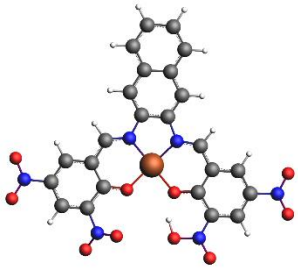	-267.288
FH-	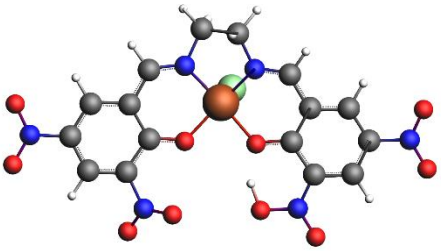	-304.457
GH-	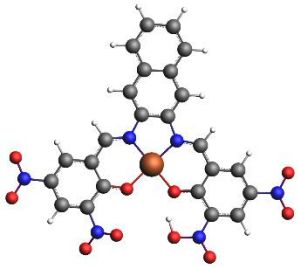	-384.127
HH-	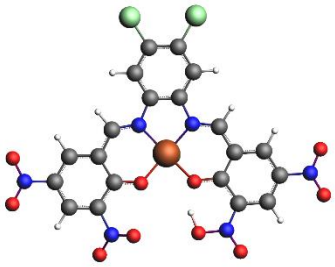	-337.535

IH-	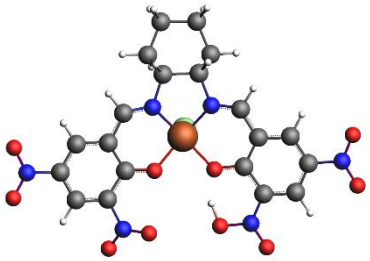	-363.073
JH-	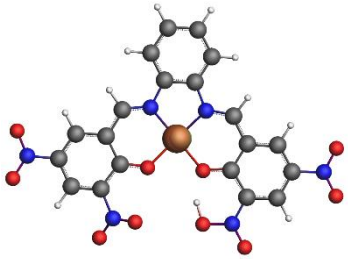	-340.557
KH-	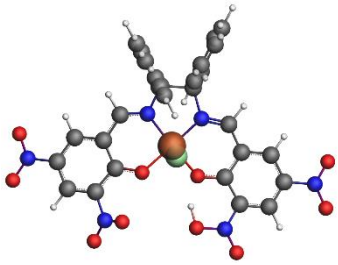	-441.834
LH-	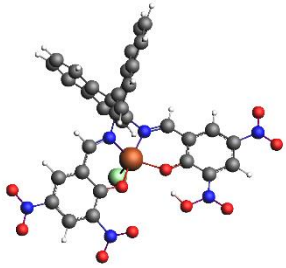	-495.863

Table 6. Molecular images and energies for catalyst species XH_2

Species	Image of Lowest Energy State	Energy (eV)
AH_2	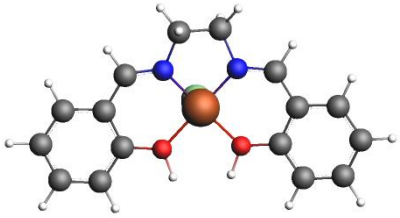	-243.333
BH_2	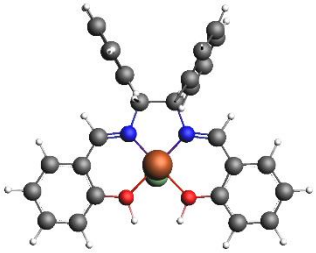	-380.580
CH_2	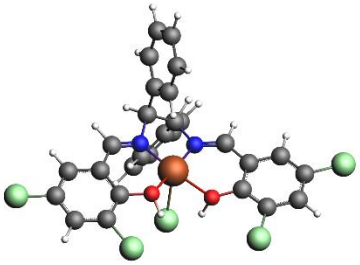	-374.003
DH_2	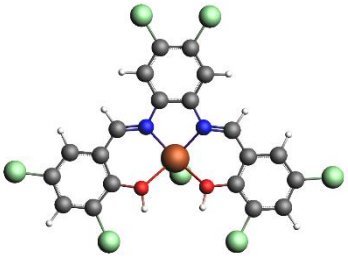	-269.700
EH_2	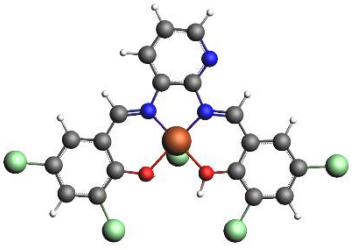	-268.156

FH_2	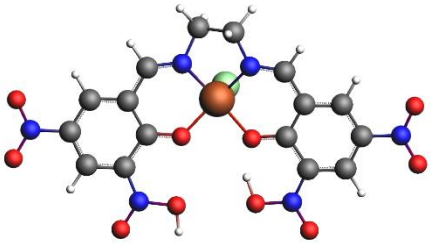	-304.709
GH_2	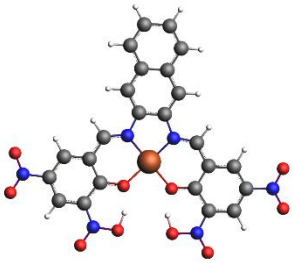	-384.339
HH_2	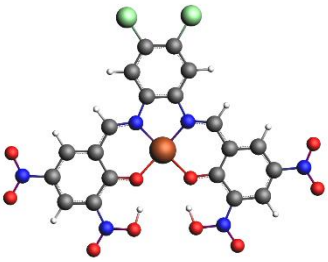	-337.714
IH_2	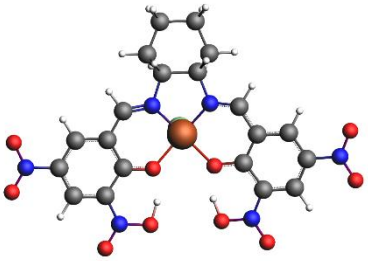	-363.467
JH_2	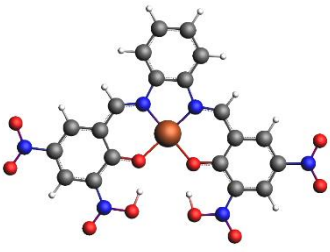	-340.768

KH_2	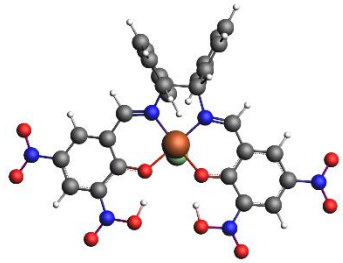	-442.091
LH_2	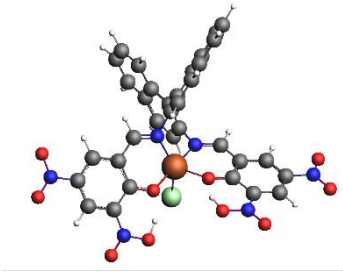	-496.334

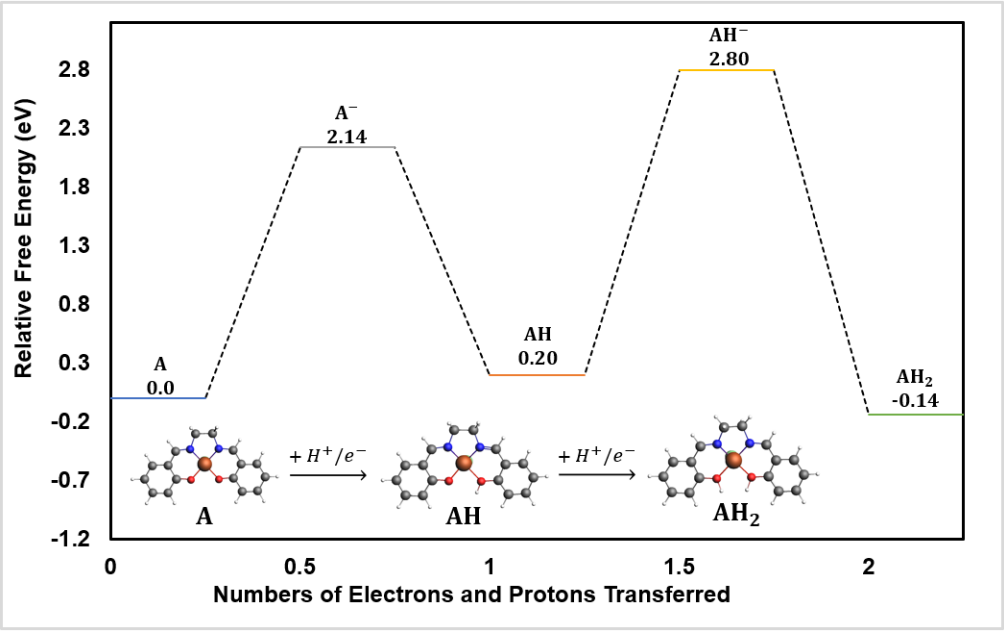

Figure 10. Reaction energy diagrams for electrochemical reduction of catalyst species A, calculated using the VASP code and model. Energies are relative to the original catalyst species at 0 V-NHE and 0 pH. Most stable configuration of each reduced intermediate is used. Atom colors are presented by gray: C, white: H, blue: N, and red: O

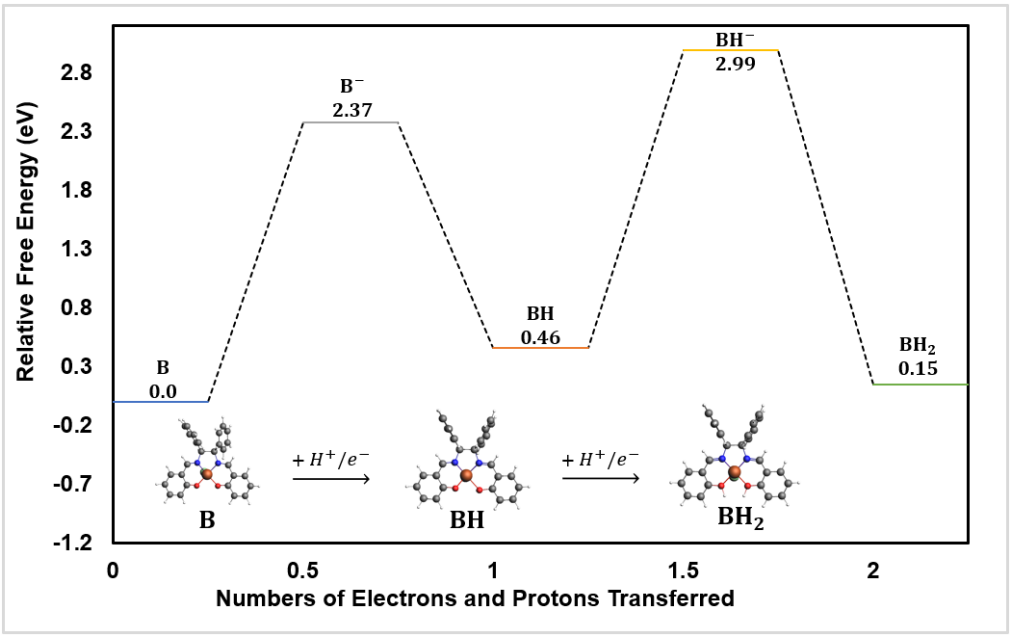

Figure 11. Reaction energy diagrams for electrochemical reduction of catalyst species B, calculated using the VASP code and model. Energies are relative to the original catalyst species at 0 V-NHE and 0 pH. Most stable configuration of each reduced intermediate is used. Atom colors are presented by gray: C, white: H, blue: N, and red: O

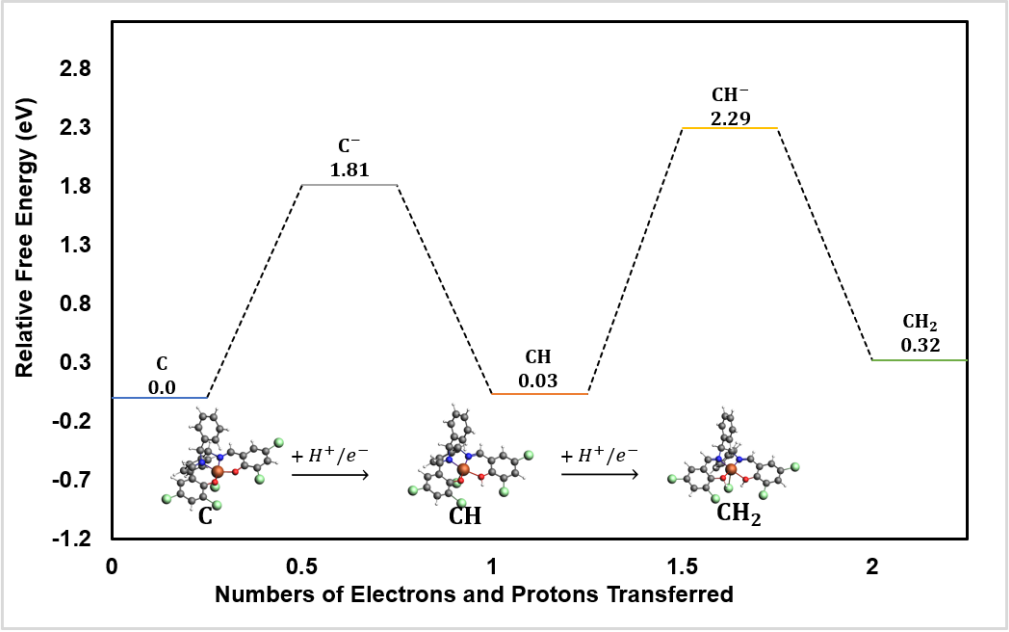

Figure 12. Reaction energy diagrams for electrochemical reduction of catalyst species C, calculated using the VASP code and model. Energies are relative to the original catalyst species at 0 V-NHE and 0 pH. Most stable configuration of each reduced intermediate is used. Atom colors are presented by gray: C, white: H, blue: N, and red: O

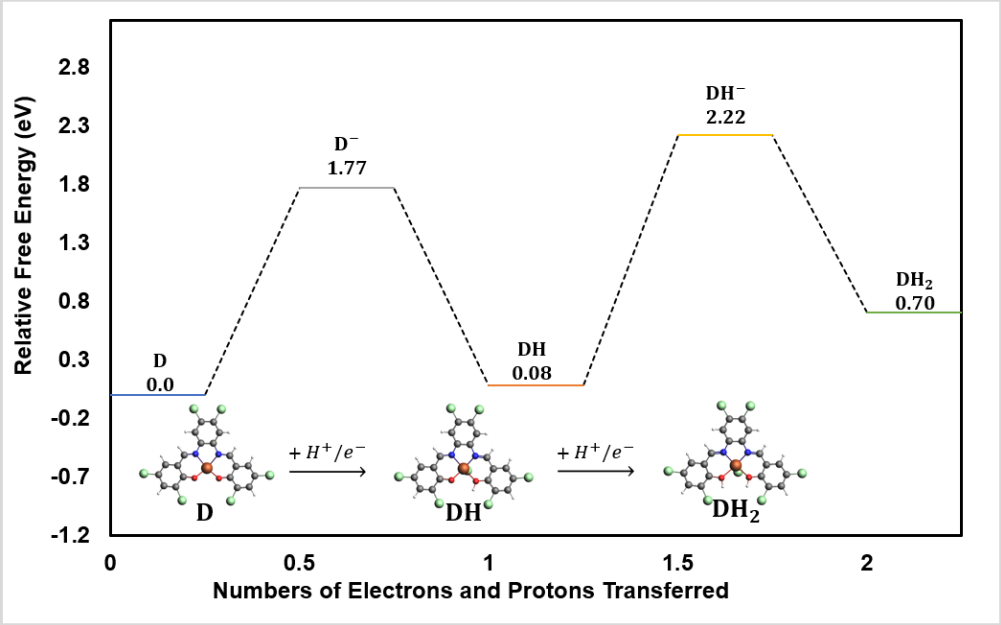

Figure 13. Reaction energy diagrams for electrochemical reduction of catalyst species D, calculated using the VASP code and model. Energies are relative to the original catalyst species at 0 V-NHE and 0 pH. Most stable configuration of each reduced intermediate is used. Atom colors are presented by gray: C, white: H, blue: N, and red: O

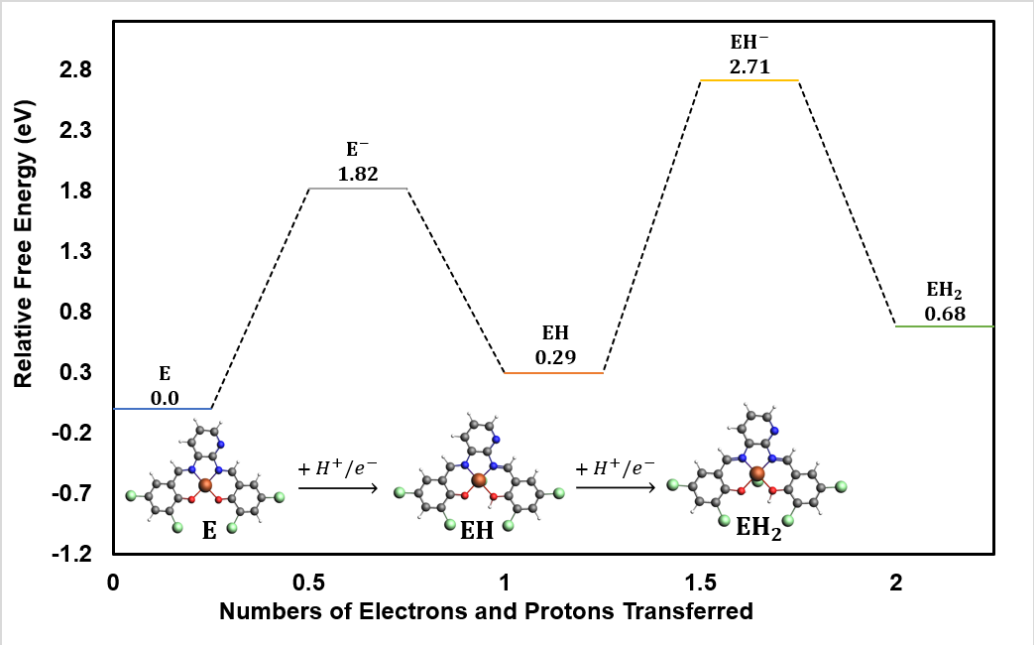

Figure 14. Reaction energy diagrams for electrochemical reduction of catalyst species E, calculated using the VASP code and model. Energies are relative to the original catalyst species at 0 V-NHE and 0 pH. Most stable configuration of each reduced intermediate is used. Atom colors are presented by gray: C, white: H, blue: N, and red: O

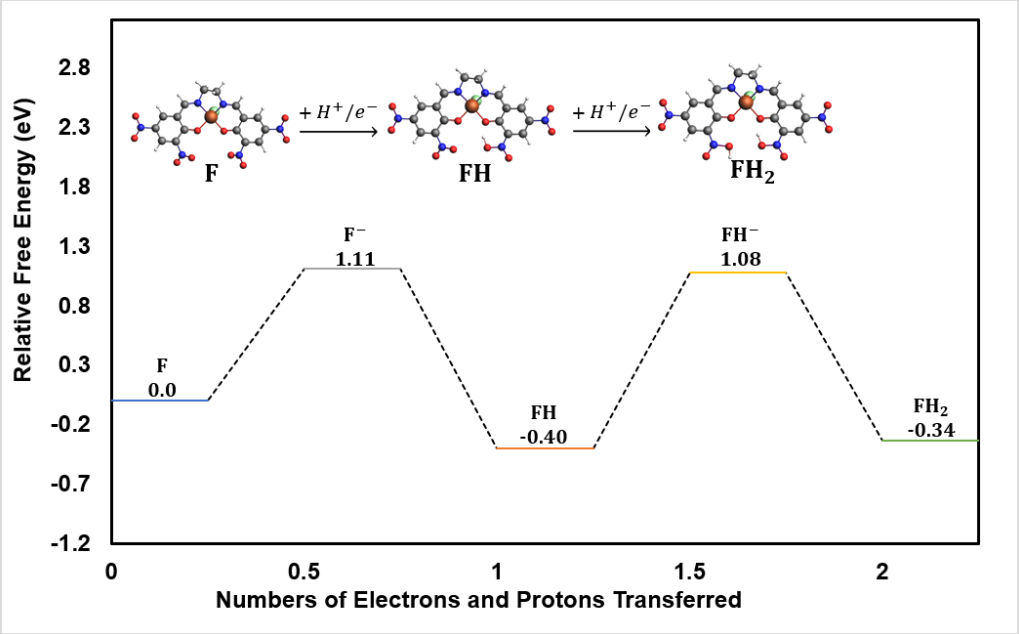

Figure 15. Reaction energy diagrams for electrochemical reduction of catalyst species F, calculated using the VASP code and model. Energies are relative to the original catalyst species at 0 V-NHE and 0 pH. Most stable configuration of each reduced intermediate is used. Atom colors are presented by gray: C, white: H, blue: N, and red: O

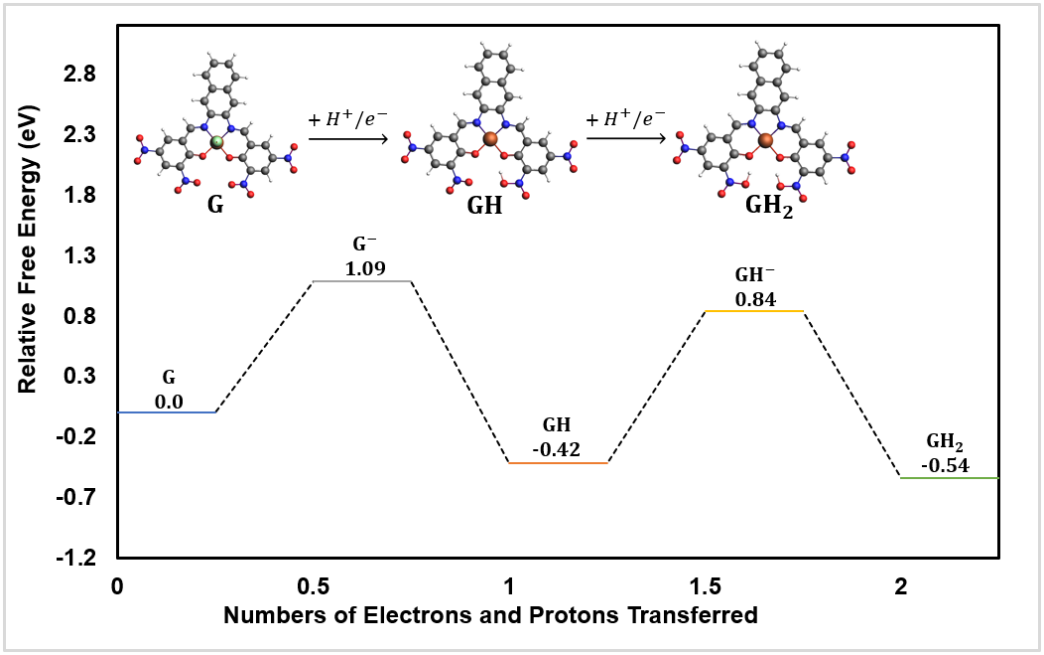

Figure 16. Reaction energy diagrams for electrochemical reduction of catalyst species G, calculated using the VASP code and model. Energies are relative to the original catalyst species at 0 V-NHE and 0 pH. Most stable configuration of each reduced intermediate is used. Atom colors are presented by gray: C, white: H, blue: N, and red: O

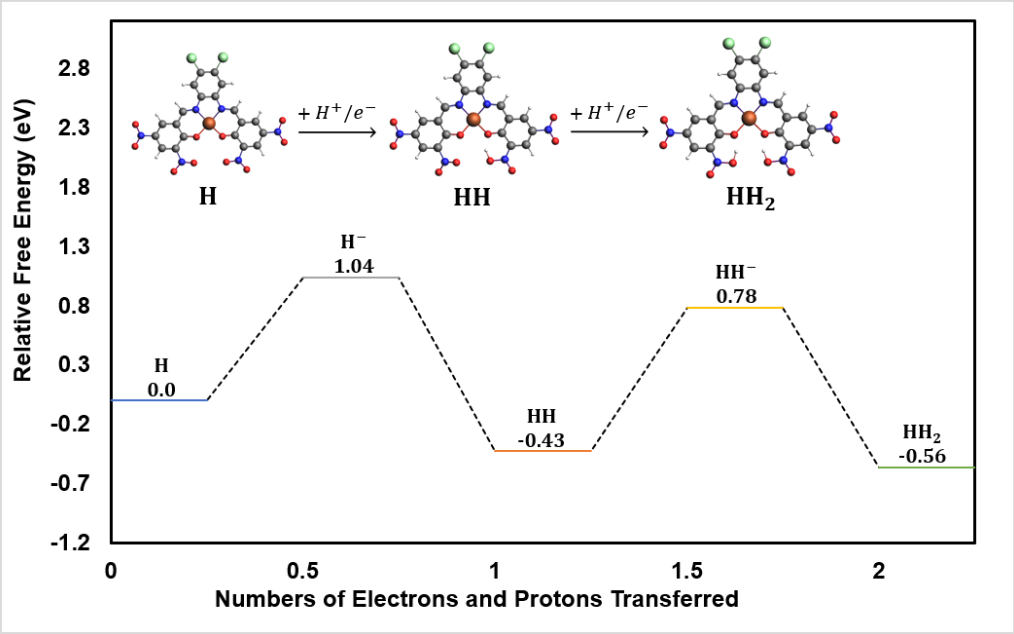

Figure 17. Reaction energy diagrams for electrochemical reduction of catalyst species H, calculated using the VASP code and model. Energies are relative to the original catalyst species at 0 V-NHE and 0 pH. Most stable configuration of each reduced intermediate is used. Atom colors are presented by gray: C, white: H, blue: N, and red: O

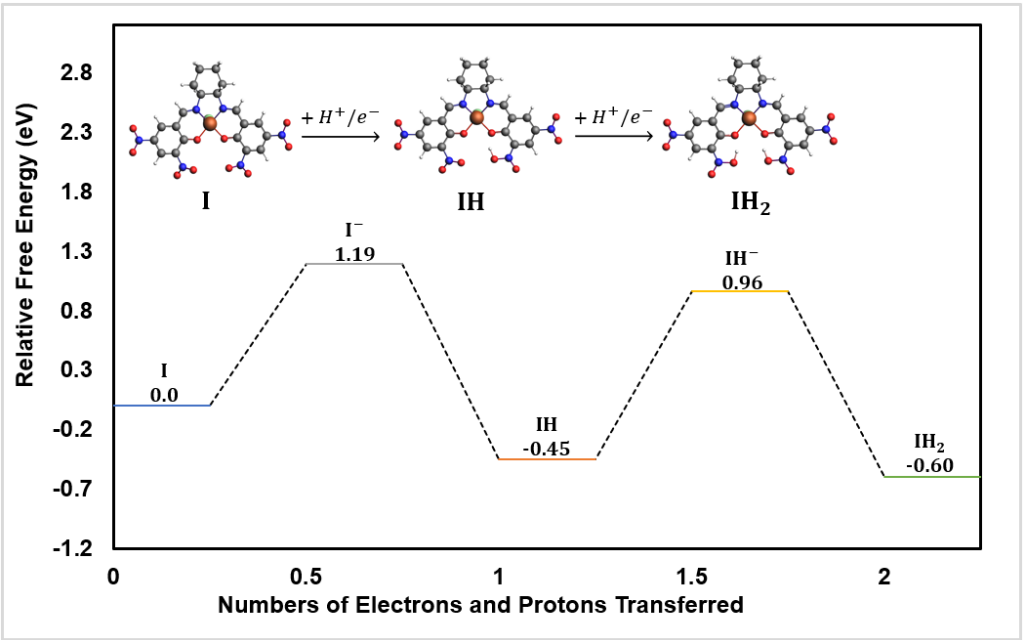

Figure 18. Reaction energy diagrams for electrochemical reduction of catalyst species I, calculated using the VASP code and model. Energies are relative to the original catalyst species at 0 V-NHE and 0 pH. Most stable configuration of each reduced intermediate is used. Atom colors are presented by gray: C, white: H, blue: N, and red: O

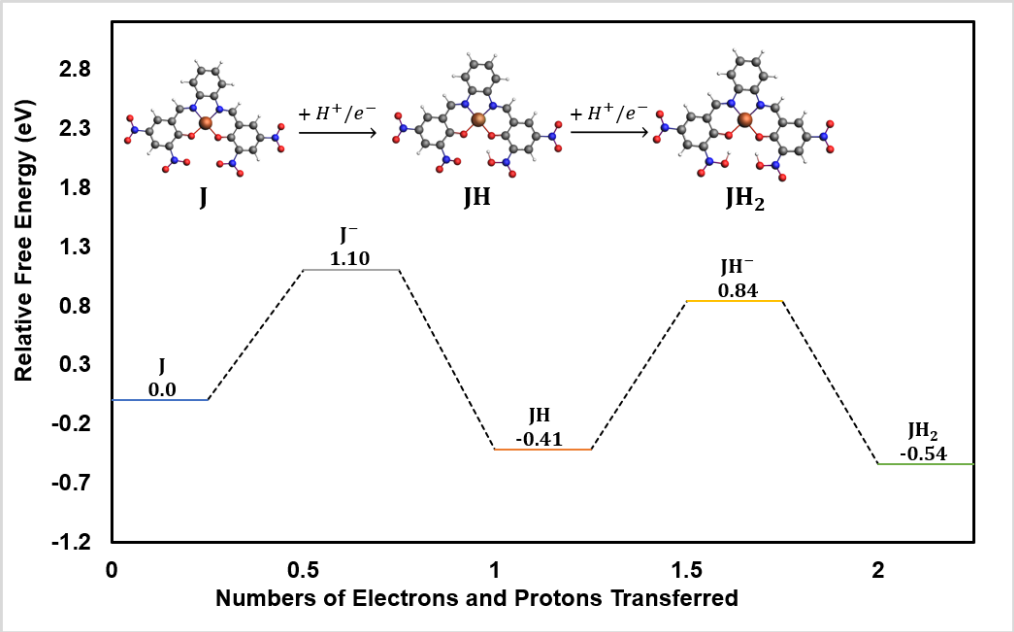

Figure 19. Reaction energy diagrams for electrochemical reduction of catalyst species J, calculated using the VASP code and model. Energies are relative to the original catalyst species at 0 V-NHE and 0 pH. Most stable configuration of each reduced intermediate is used. Atom colors are presented by gray: C, white: H, blue: N, and red: O

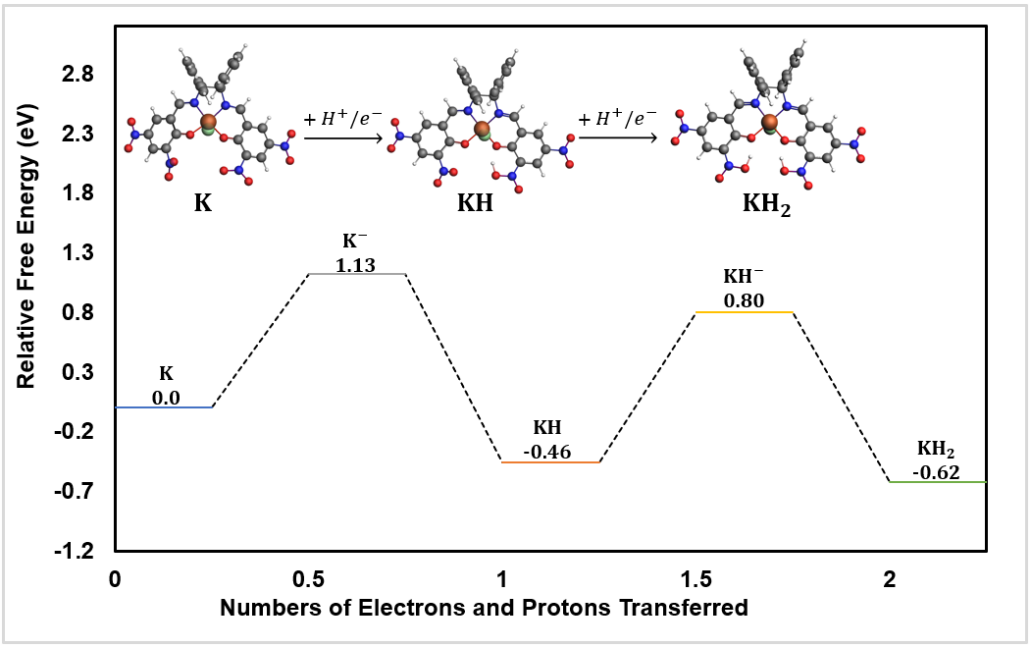

Figure 20. Reaction energy diagrams for electrochemical reduction of catalyst species K, calculated using the VASP code and model. Energies are relative to the original catalyst species at 0 V-NHE and 0 pH. Most stable configuration of each reduced intermediate is used. Atom colors are presented by gray: C, white: H, blue: N, and red: O

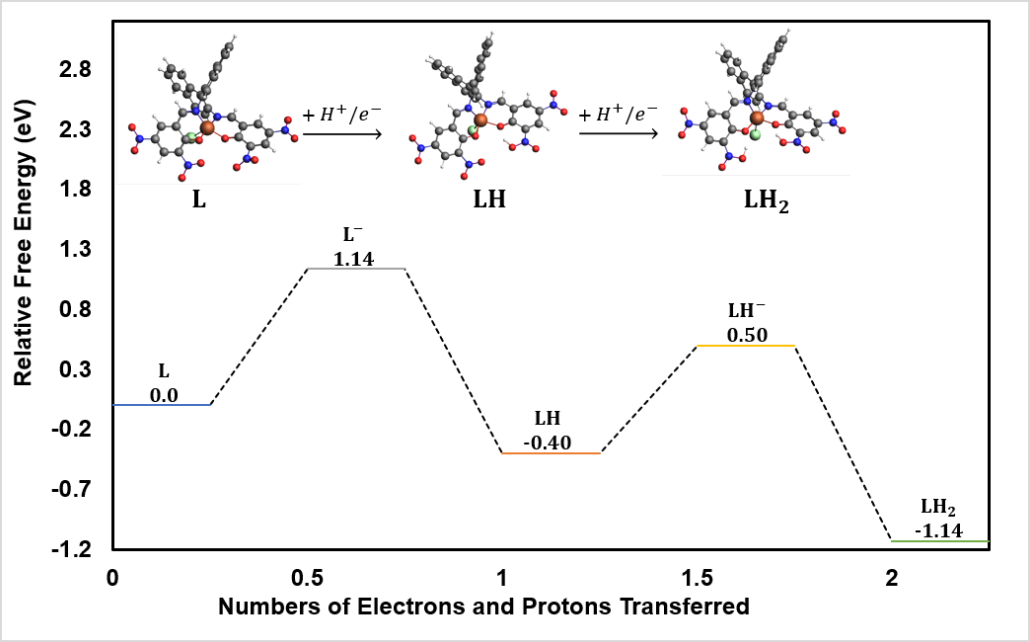

Figure 21. Reaction energy diagrams for electrochemical reduction of catalyst species L, calculated using the VASP code and model. Energies are relative to the original catalyst species at 0 V-NHE and 0 pH. Most stable configuration of each reduced intermediate is used. Atom colors are presented b gray: C, white: H, blue: N, and red: O

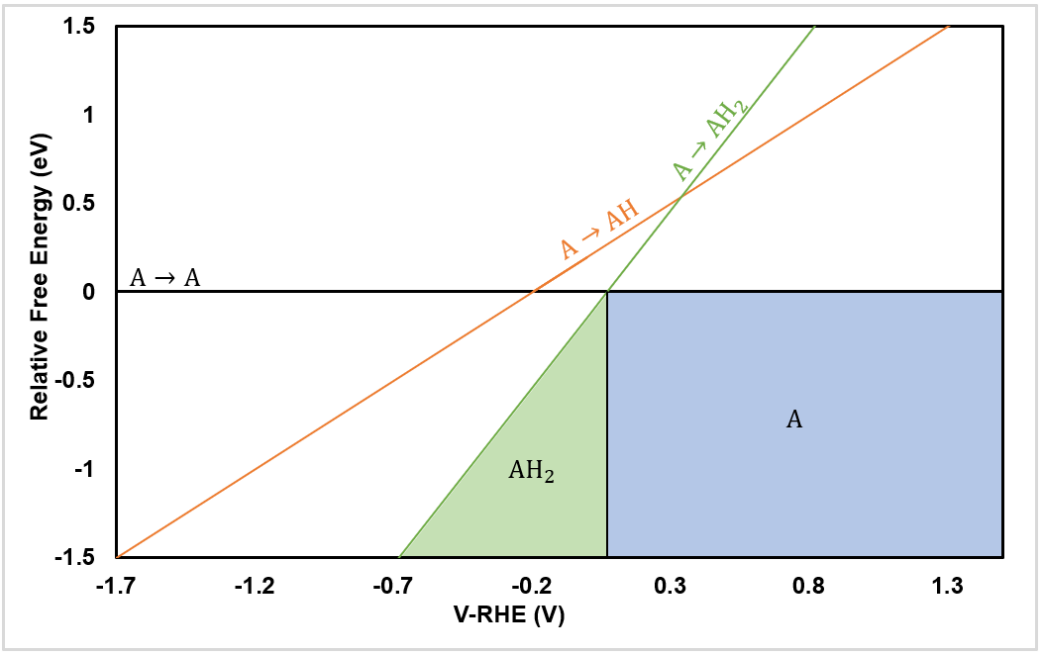

Figure 22. Relative energy potential differences of coupled proton-electron transfers on a V-RHE scale at pH = 0 with favorable species regions for catalyst A

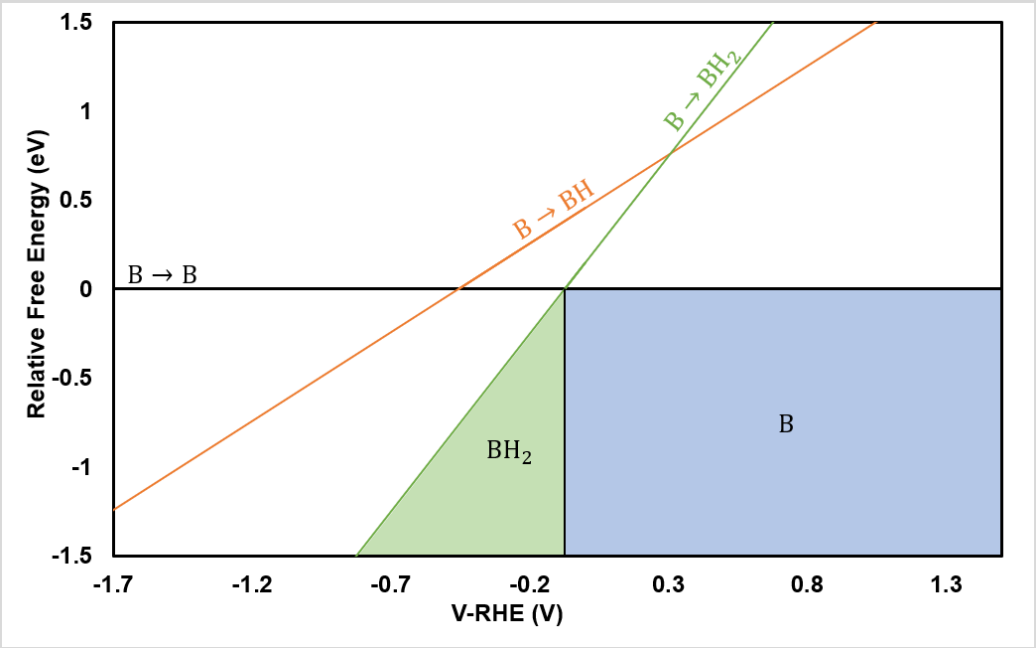

Figure 23. Relative energy potential differences of coupled proton-electron transfers on a V-RHE scale at pH = 0 with favorable species regions for catalyst B

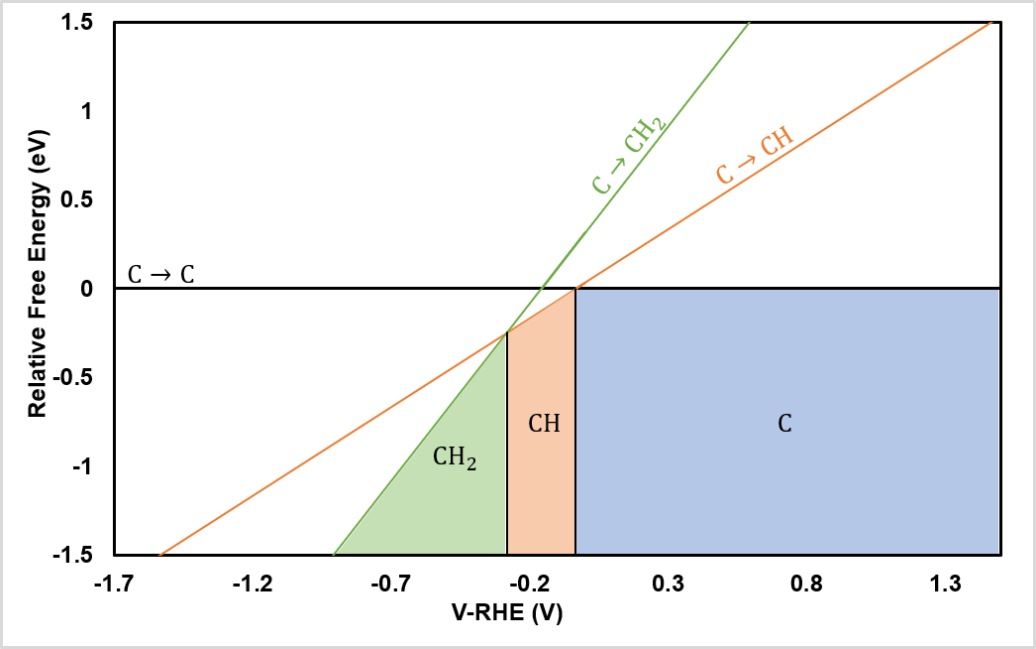

Figure 24. Relative energy potential differences of coupled proton-electron transfers on a V-RHE scale at pH = 0 with favorable species regions for catalyst C

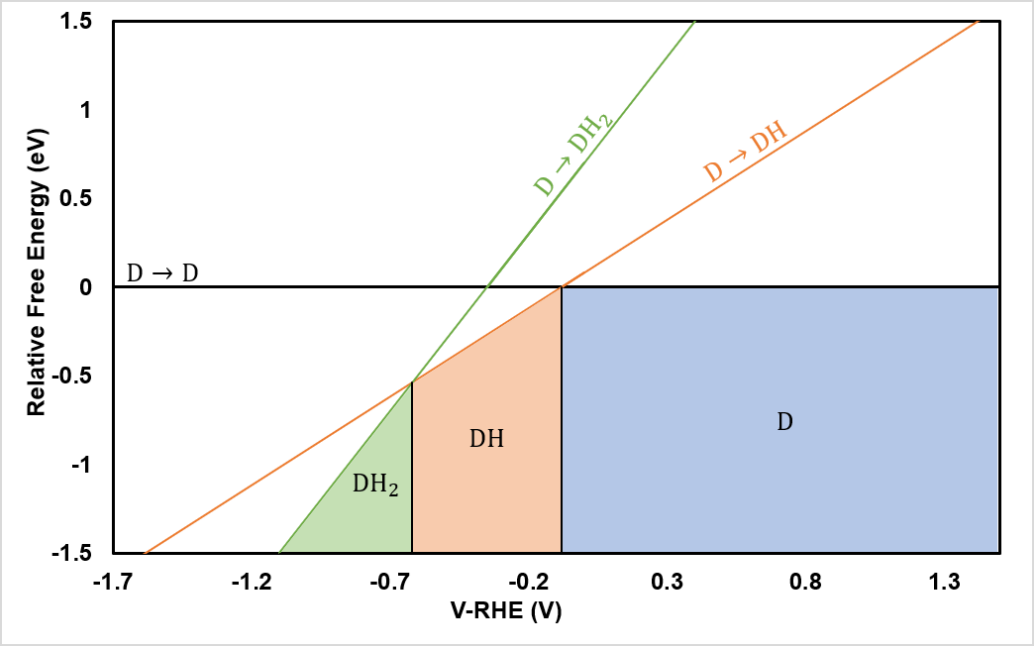

Figure 25. Relative energy potential differences of coupled proton-electron transfers on a V-RHE scale at pH = 0 with favorable species regions for catalyst D

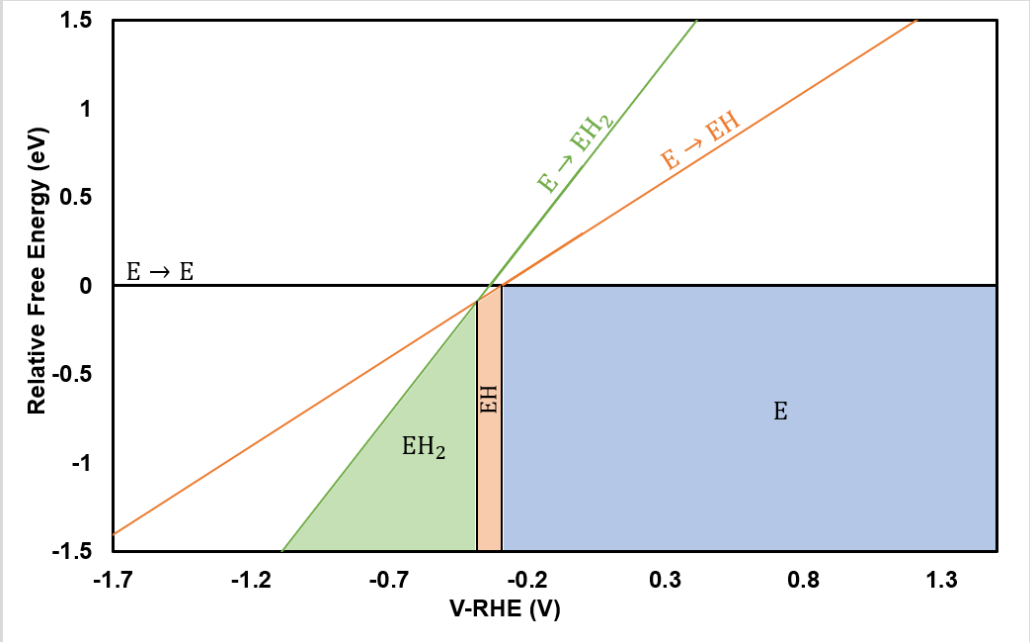

Figure 26. Relative energy potential differences of coupled proton-electron transfers on a V-RHE scale at pH = 0 with favorable species regions for catalyst E

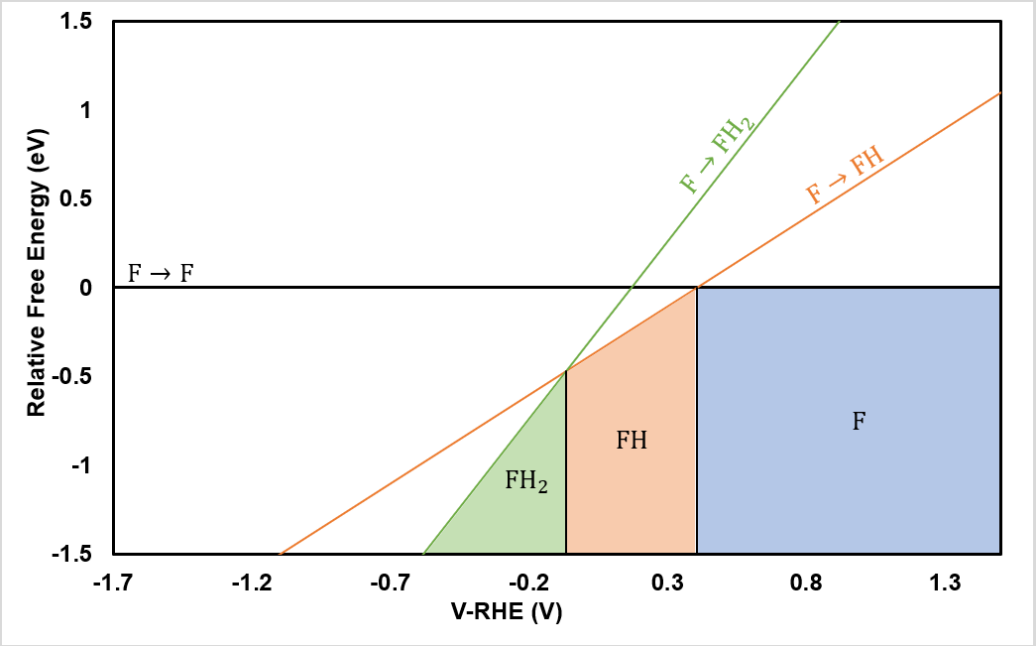

Figure 27. Relative energy potential differences of coupled proton-electron transfers on a V-RHE scale at pH = 0 with favorable species regions for catalyst F

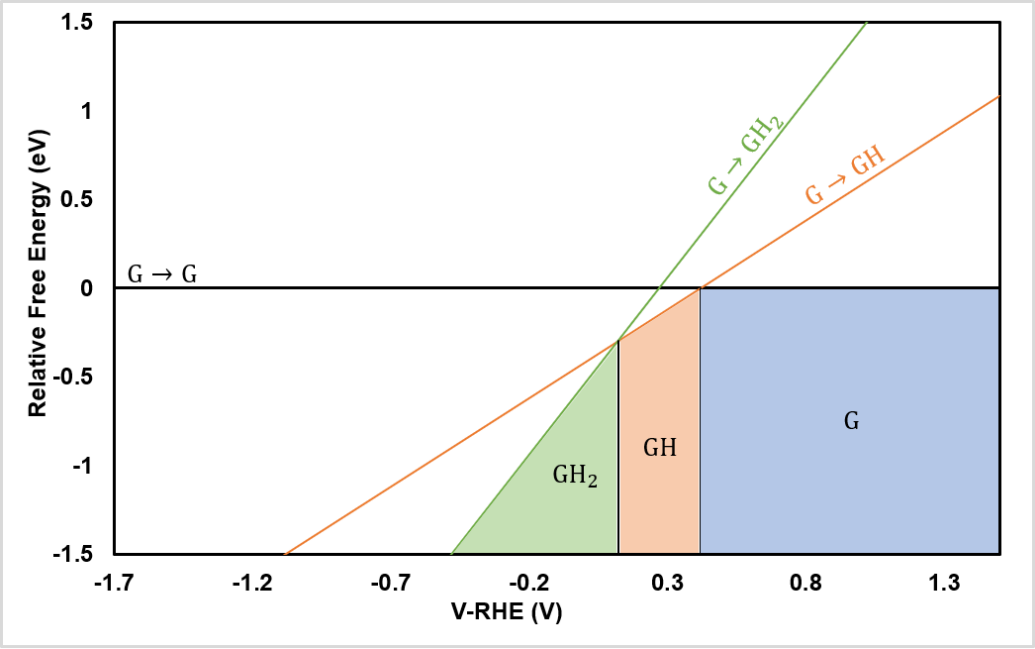

Figure 28. Relative energy potential differences of coupled proton-electron transfers on a V-RHE scale at pH = 0 with favorable species regions for catalyst G

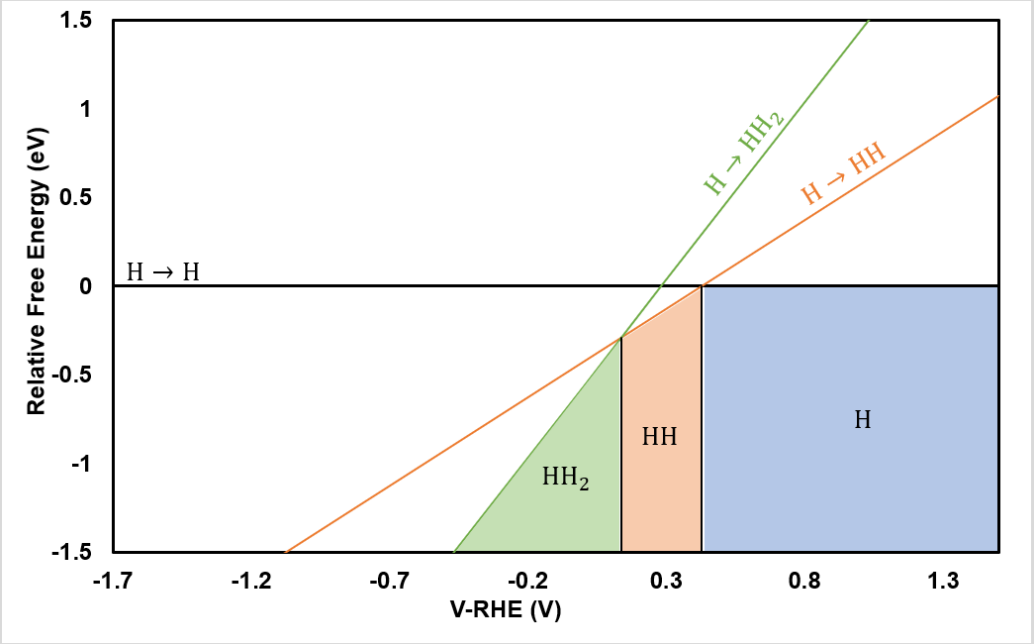

Figure 29. Relative energy potential differences of coupled proton-electron transfers on a V-RHE scale at pH = 0 with favorable species regions for catalyst H

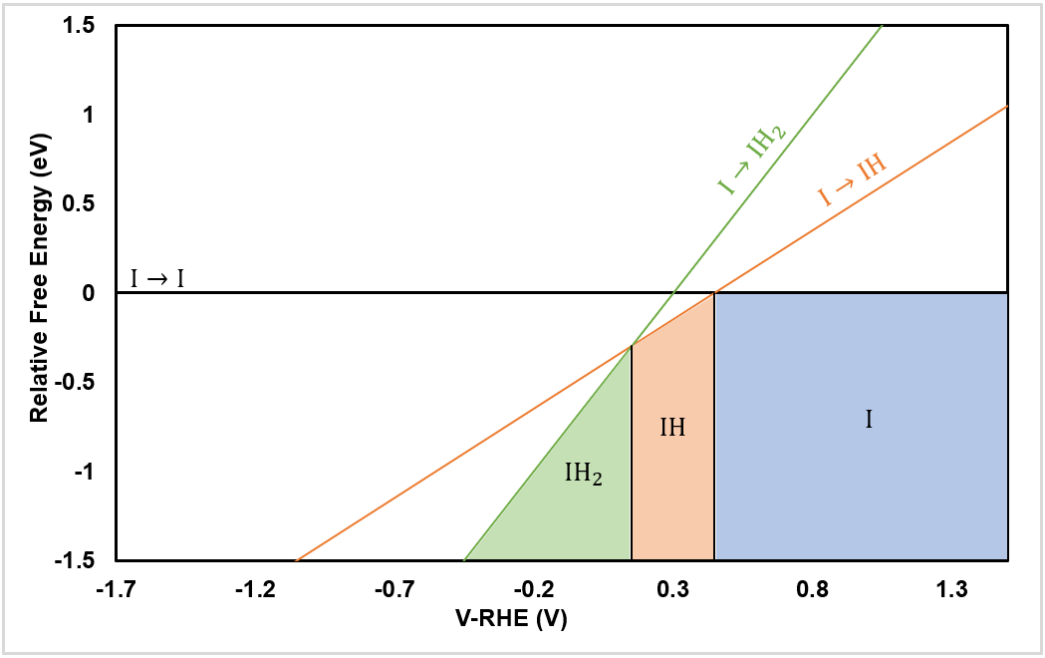

Figure 30. Relative energy potential differences of coupled proton-electron transfers on a V-RHE scale at pH = 0 with favorable species regions for catalyst I

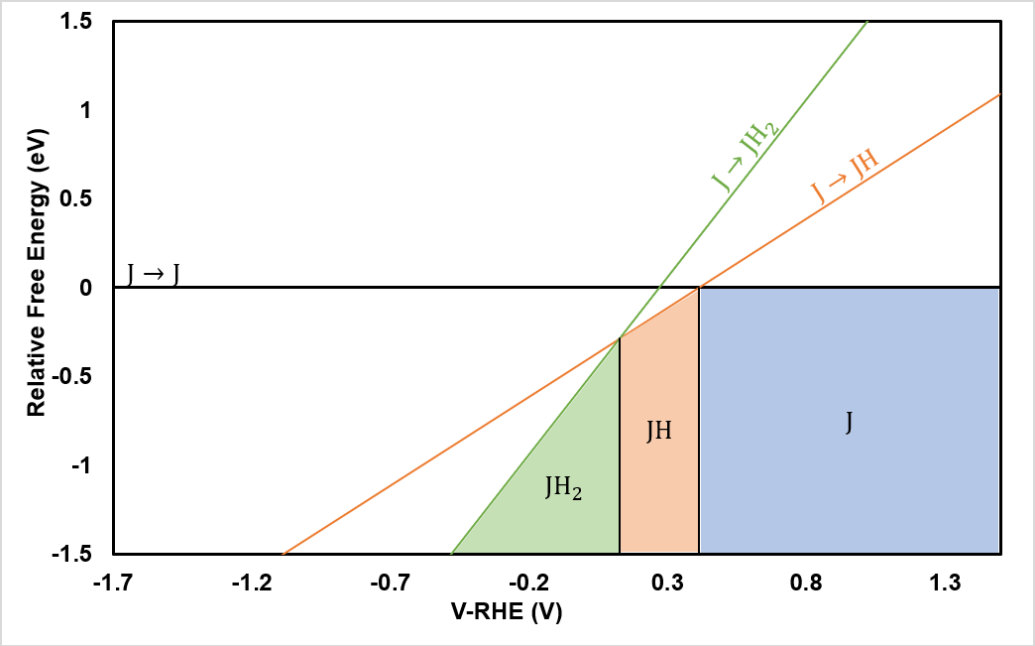

Figure 31. Relative energy potential differences of coupled proton-electron transfers on a V-RHE scale at pH = 0 with favorable species regions for catalyst J

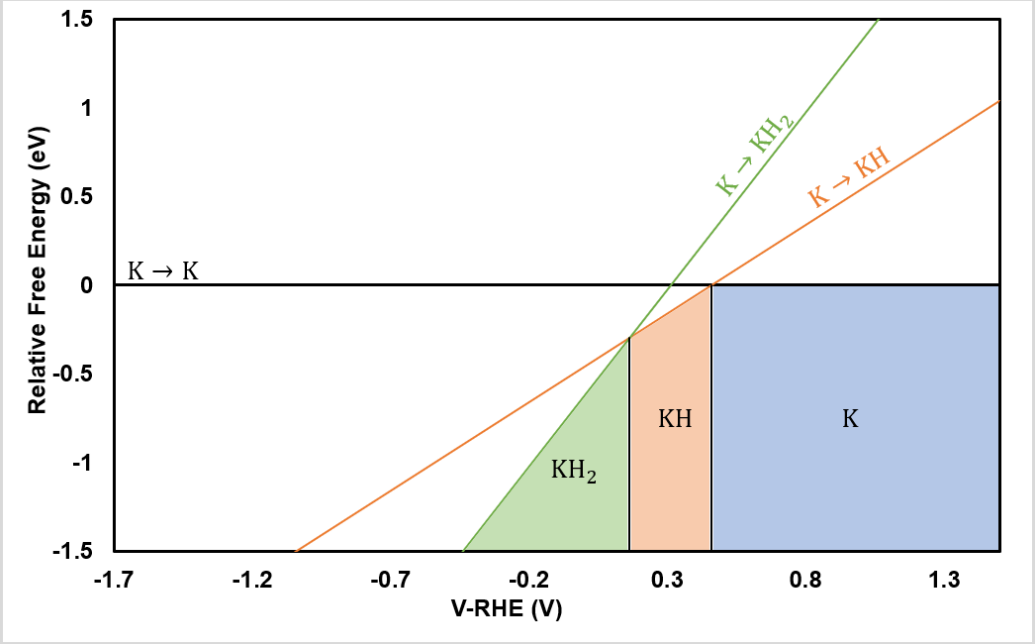

Figure 32. Relative energy potential differences of coupled proton-electron transfers on a V-RHE scale at pH = 0 with favorable species regions for catalyst K

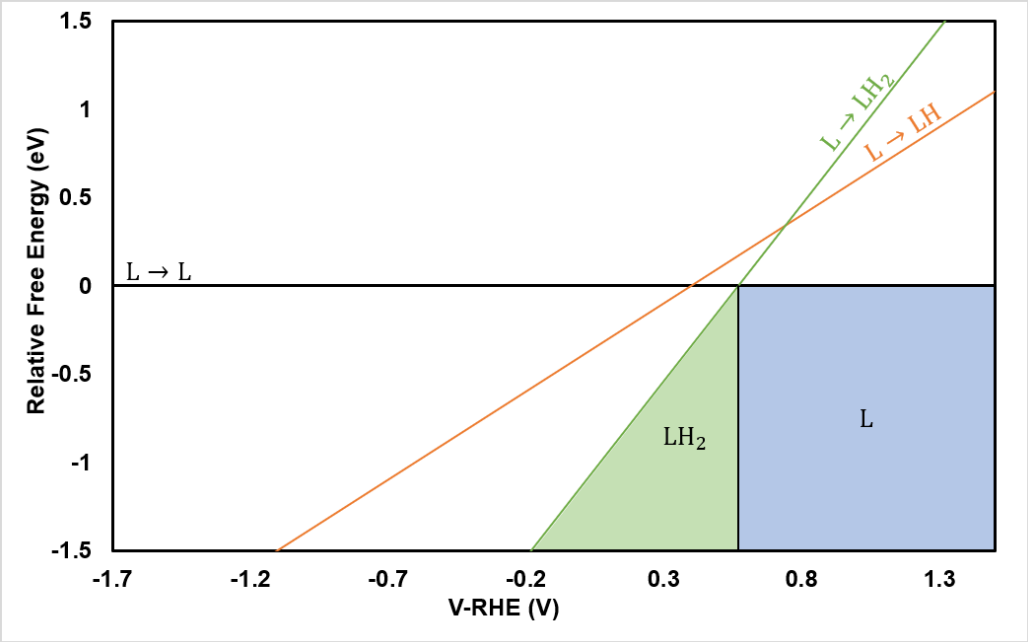

Figure 33. Relative energy potential differences of coupled proton-electron transfers on a V-RHE scale at pH = 0 with favorable species regions for catalyst L

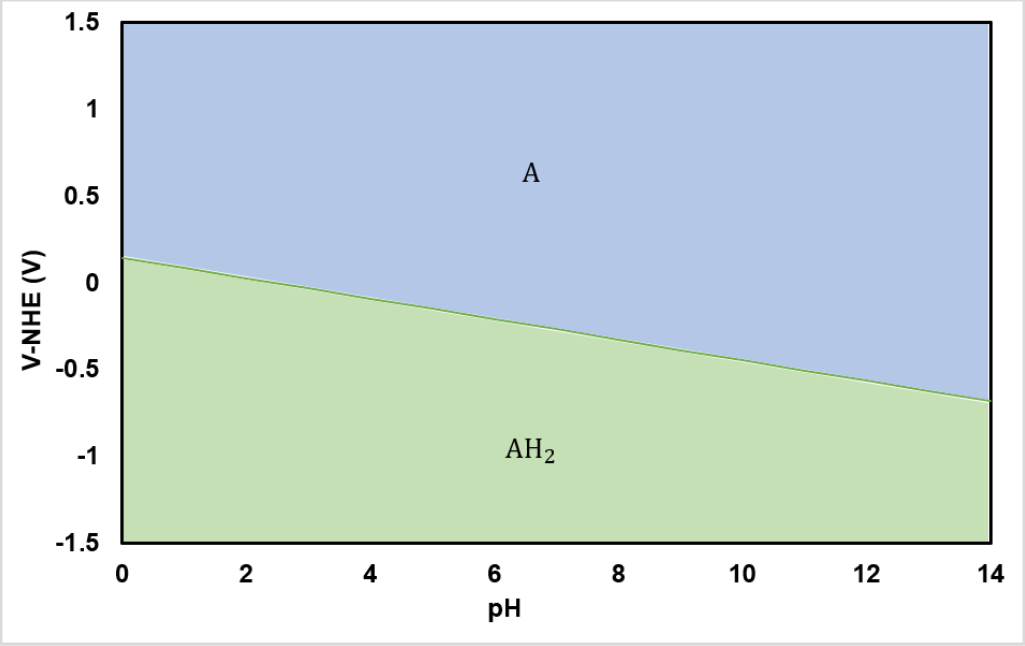

Figure 34. Relative energy potential differences of reaction mechanism steps on a V-NHE scale with favorable species regions versus pH conditions with favorable species regions for catalyst A

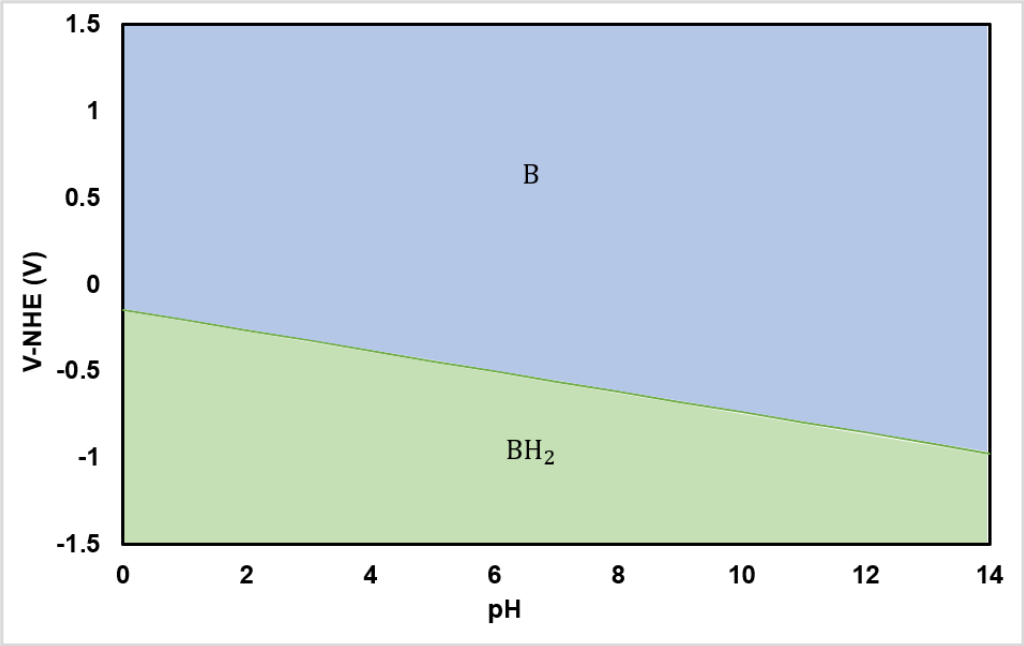

Figure 35. Relative energy potential differences of reaction mechanism steps on a V-NHE scale with favorable species regions versus pH conditions with favorable species regions for catalyst B

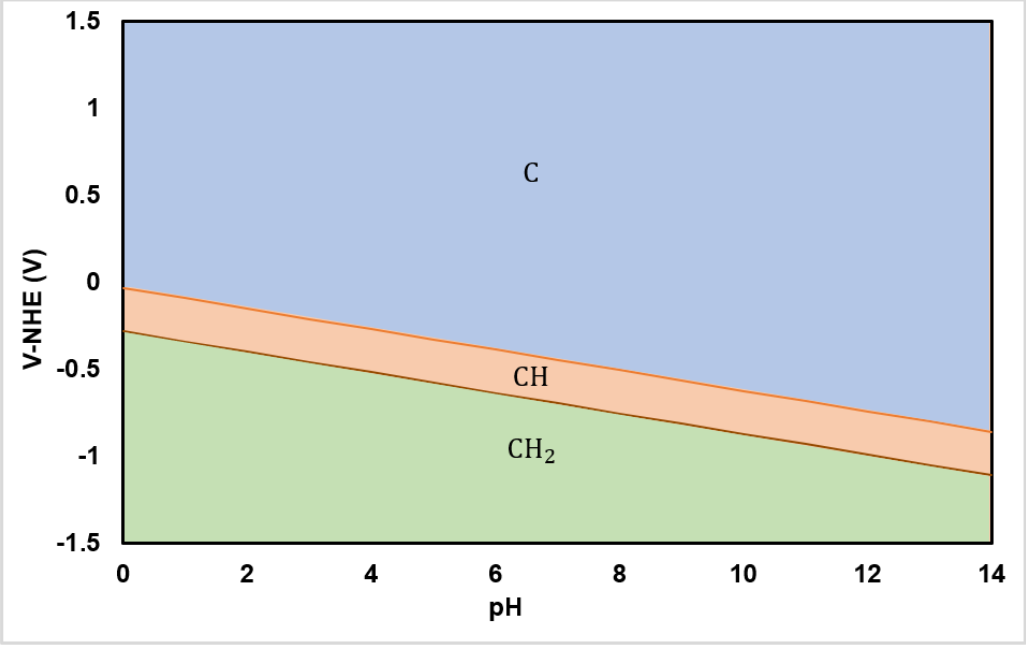

Figure 36. Relative energy potential differences of reaction mechanism steps on a V-NHE scale with favorable species regions versus pH conditions with favorable species regions for catalyst C

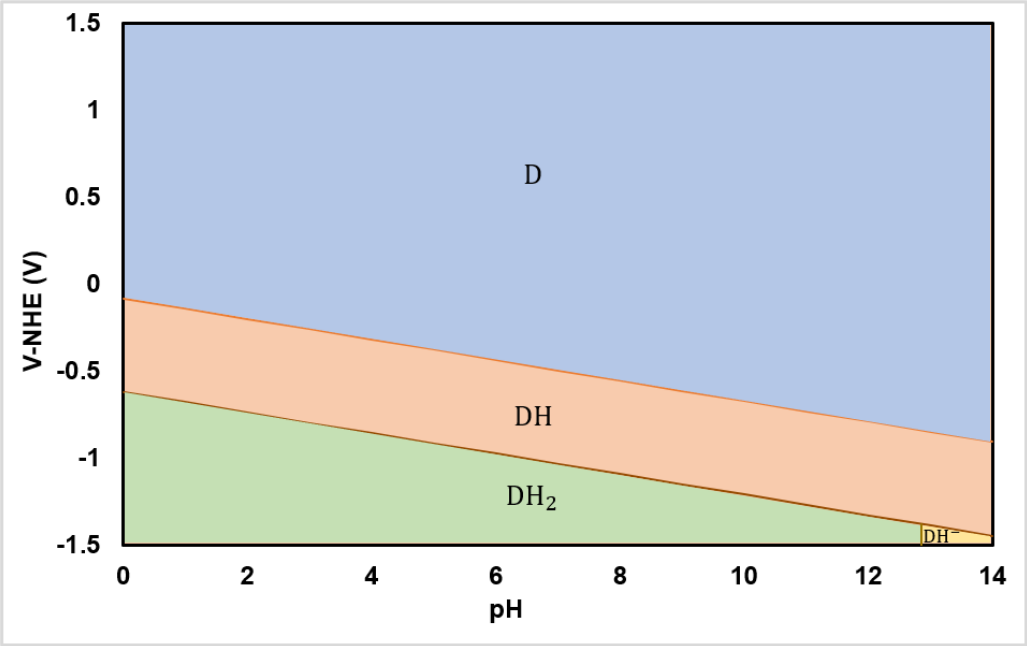

Figure 37. Relative energy potential differences of reaction mechanism steps on a V-NHE scale with favorable species regions versus pH conditions with favorable species regions for catalyst D

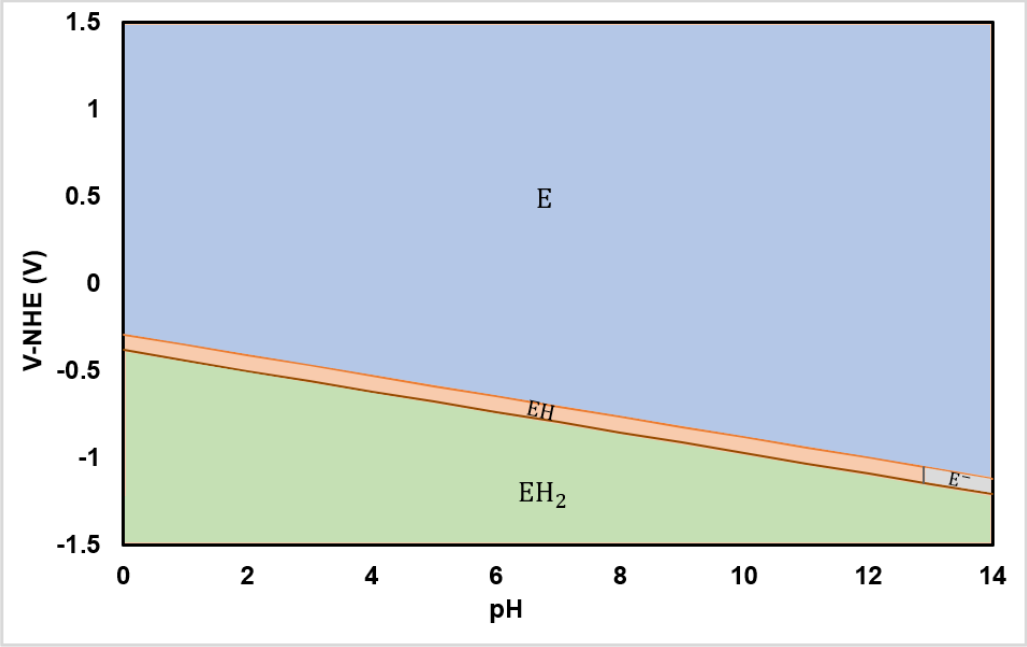

Figure 38. Relative energy potential differences of reaction mechanism steps on a V-NHE scale with favorable species regions versus pH conditions with favorable species regions for catalyst E

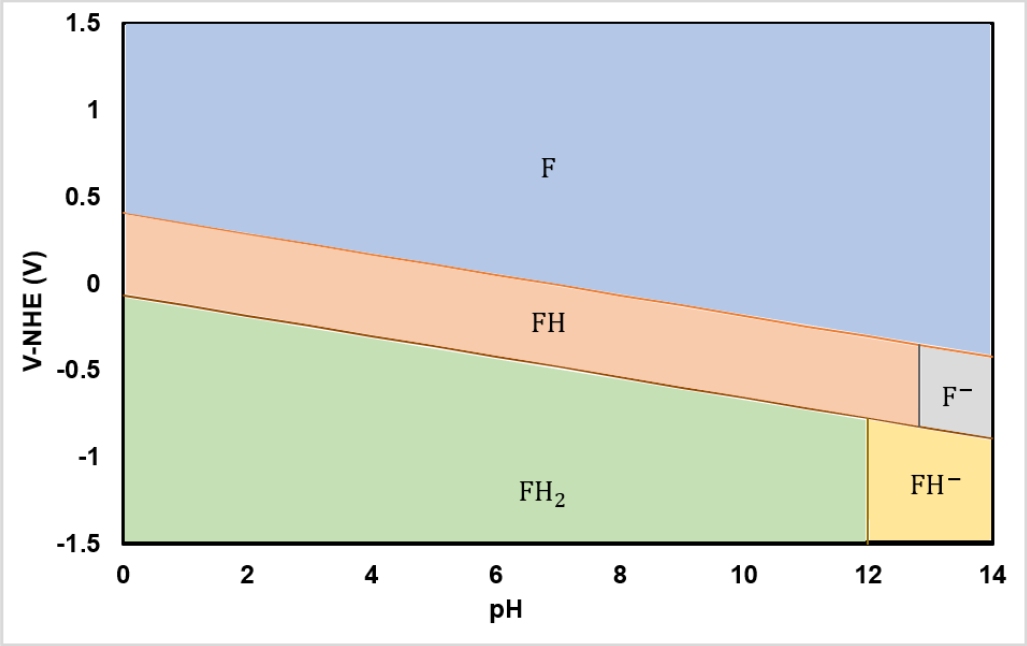

Figure 39. Relative energy potential differences of reaction mechanism steps on a V-NHE scale with favorable species regions versus pH conditions with favorable species regions for catalyst F

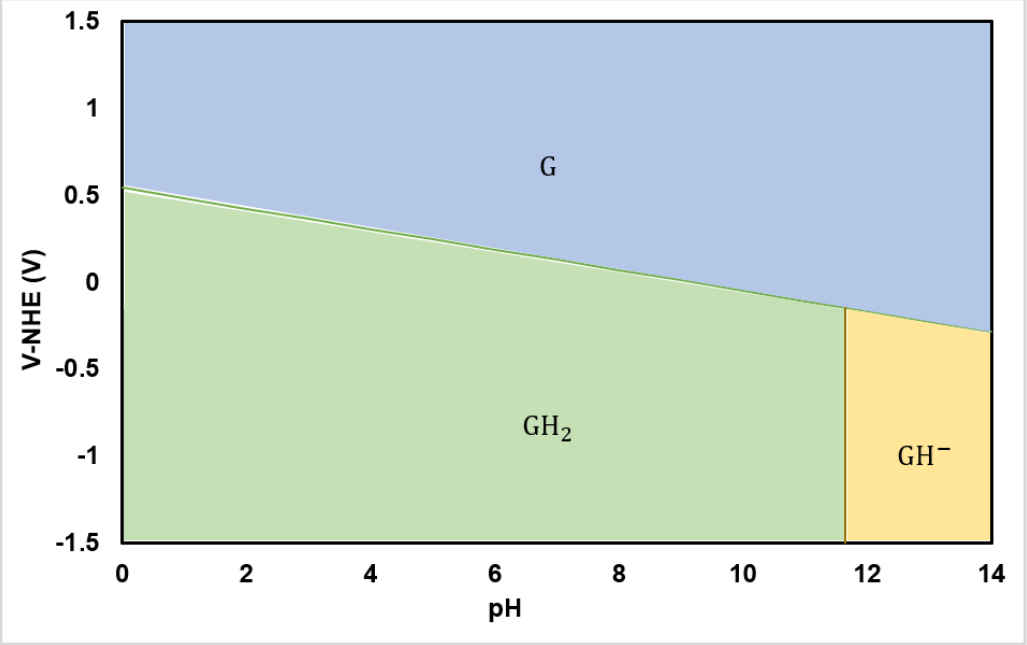

Figure 40. Relative energy potential differences of reaction mechanism steps on a V-NHE scale with favorable species regions versus pH conditions with favorable species regions for catalyst G

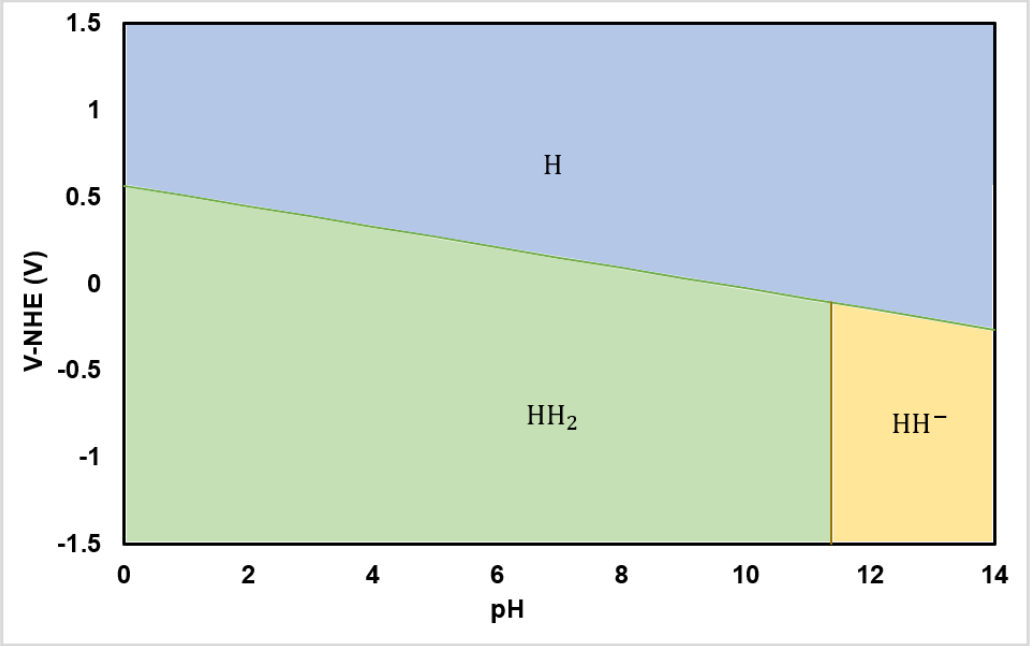

Figure 41. Relative energy potential differences of reaction mechanism steps on a V-NHE scale with favorable species regions versus pH conditions with favorable species regions for catalyst H

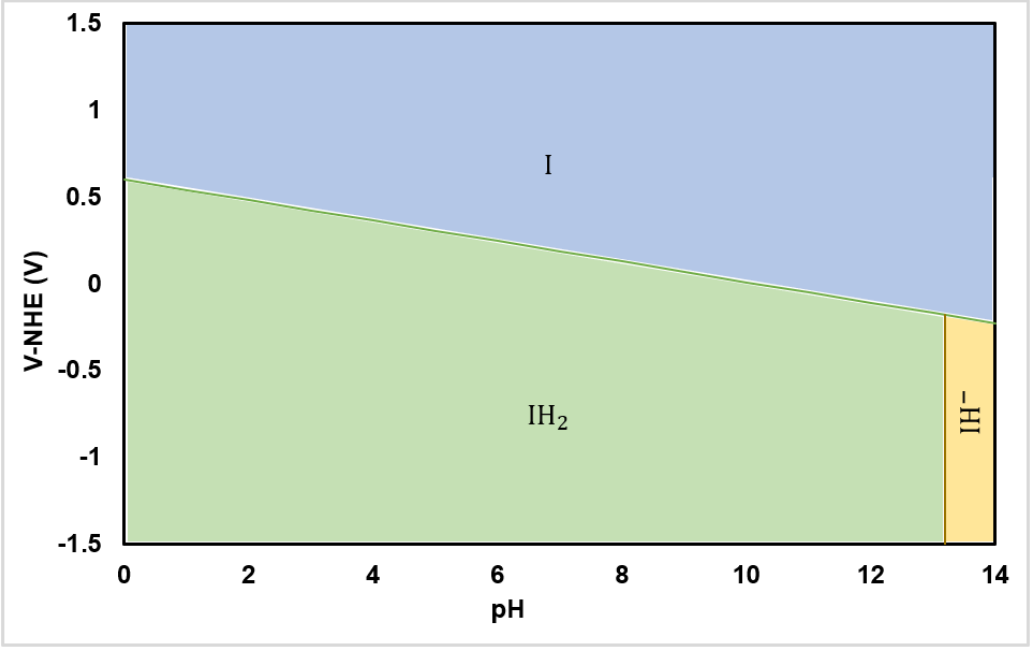

Figure 42. Relative energy potential differences of reaction mechanism steps on a V-NHE scale with favorable species regions versus pH conditions with favorable species regions for catalyst I

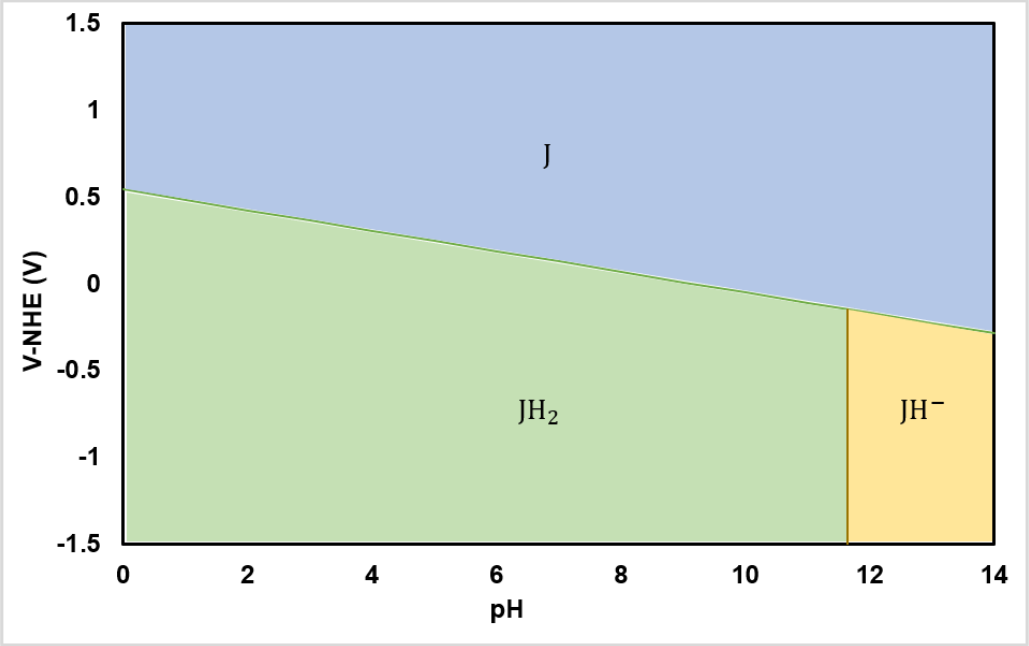

Figure 43. Relative energy potential differences of reaction mechanism steps on a V-NHE scale with favorable species regions versus pH conditions with favorable species regions for catalyst J

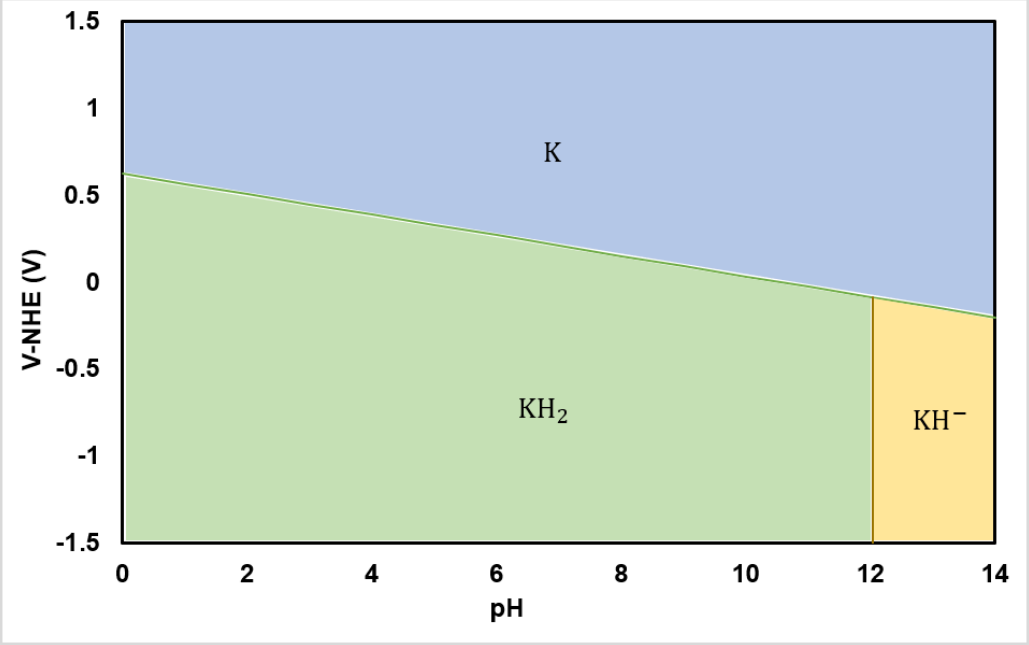

Figure 44. Relative energy potential differences of reaction mechanism steps on a V-NHE scale with favorable species regions versus pH conditions with favorable species regions for catalyst K

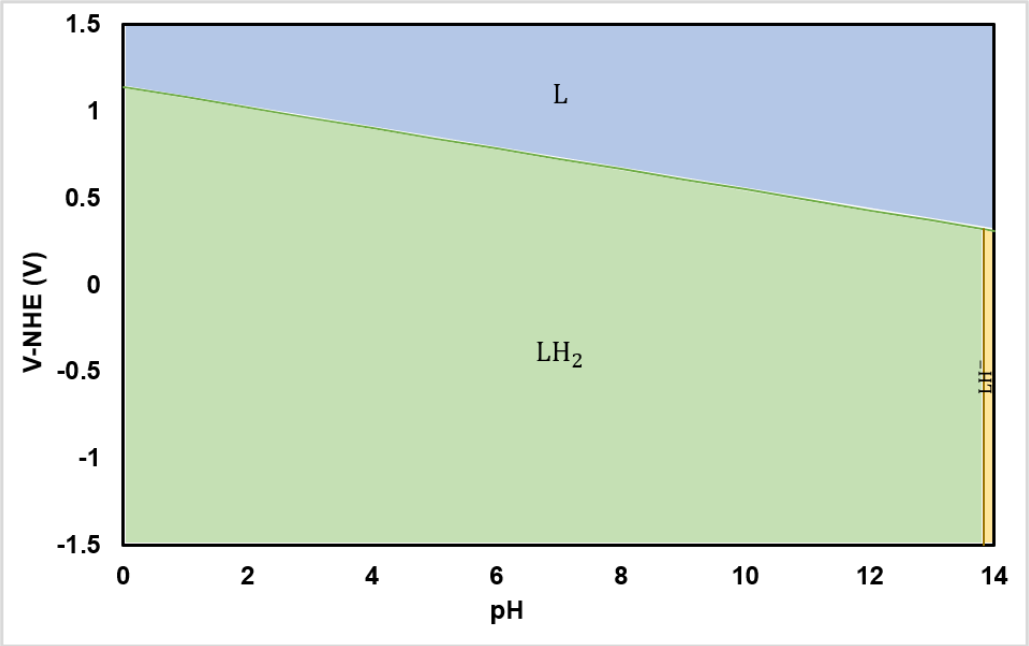

Figure 45. Relative energy potential differences of reaction mechanism steps on a V-NHE scale with favorable species regions versus pH conditions with favorable species regions for catalyst L

BIBLIOGRAPHY

1. Chantarojsiri, T., Ziller, J. W., & Yang, J. Y. (2018). Incorporation of redox-inactive cations promotes iron catalyzed aerobic C–H oxidation at mild potentials. *Chemical Science*, *9*(9), 2567–2574. https://doi.org/10.1039/c7sc04486k
2. Çakmak, D., Çakran, S., Yalçinkaya, S., & Demetgül, C. (2017). Synthesis of salen-type Schiff base metal complexes, electropolymerization on graphite electrode surface and investigation of electrocatalytic effects. *Journal of Electroanalytical Chemistry*, *808*, 65–74. https://doi.org/10.1016/j.jelechem.2017.11.058
3. Bose, P., Mukherjee, C., & Golder, A. K. (2019). A NIII complex of the tetradentate Salen Ligand H2LNH2 comprising an anchoring –NH2 group: Synthesis, characterization and electrocatalytic CO2 reduction to alcohols. *Inorganic Chemistry Frontiers*, *6*(7), 1721–1728. https://doi.org/10.1039/c9qi00353c
4. Sheng, X., Alvarez-Gallego, Y., Dominguez-Benetton, X., Baert, K., Hubin, A., Zhao, H., Mihaylov, T. T., Pierloot, K., Vankelecom, I. F. J., & Pescarmona, P. P. (2018). Carbon-supported iron complexes as electrocatalysts for the cogeneration of hydroxylamine and electricity in a no-H2 fuel cell: A combined electrochemical and density functional theory study. *Journal of Power Sources*, *390*, 249–260. https://doi.org/10.1016/j.jpowsour.2018.04.040
5. Li, C. B., Chu, Y., He, J., Xie, J., Liu, J., Wang, N., & Tang, J. (2019). Photocatalytic hydrogen production based on a serial metal-salen complexes and the reaction mechanism. *ChemCatChem*, *11*(24), 6324–6331. https://doi.org/10.1002/cctc.201901656
6. Wang, J., Yuan, Z., Nie, R., Hou, Z., & Zheng, X. (2010). Hydrogenation of nitrobenzene to aniline over silica gel supported nickel catalysts. *Industrial & Engineering Chemistry Research*, *49*(10), 4664–4669. https://doi.org/10.1021/ie1002069
7. Senthamarai, T., Chandrashekhar, V. G., Gawande, M. B., Kalevaru, N. V., Zbořil, R., Kamer, P. C., Jagadeesh, R. V., & Beller, M. (2020). Ultra-small cobalt nanoparticles from molecularly-defined co–salen complexes for catalytic synthesis of amines. *Chemical Science*, *11*(11), 2973–2981. https://doi.org/10.1039/c9sc04963k
8. Venkataramanan, N. S., Kuppuraj, G., & Rajagopal, S. (2005). Metal–salen complexes as efficient catalysts for the oxygenation of heteroatom containing organic compounds—synthetic and mechanistic aspects. *Coordination Chemistry Reviews*, *249*(11-12), 1249–1268. https://doi.org/10.1016/j.ccr.2005.01.023
9. Böttcher, A., Grinstaff, M. W., Labinger, J. A., & Gray, H. B. (1996). Aerobic oxidation of hydrocarbons catalyzed by electronegative iron salen complexes. *Journal of Molecular Catalysis A: Chemical*, *113*, 191–200. https://doi.org/https://doi.org/10.1016/S1381-1169(96)00053-2
10. Kresse, G., & Furthmüller, J. (1996). Efficient iterative schemes for ab initio total-energy calculations using a plane-wave basis set. *Phys. Rev. B.*, *54*, 11169—11186.
11. Kresse, G., & Furthmüller, J. (1996). Efficiency of ab-initio energy calculations for metals and semiconductors using a plane-wave basis set. *Computational Materials Science, 6*, 15—50.
12. Kresse, G., & Hafner, J. (1993). Ab initio molecular dynamics for liquid metals. *Phys. Rev. B.*, *47*, 558—561.
13. Blöchl, P.E. (1994). Projector augmented-wave method. *Phys. Rev. B.*, *50*, 17953—17979.

14. Perdew, J.P., Burke, K., & Ernzerhof, M. (1997). Generalized Gradient Approximation Made Simple. *Phys. Rev. Lett., 77,* 3865—3868.
15. Monkhorst, H.J., & Pack, J.D. (1976). Special points for Brillouin-zone integrations. *Phys. Rev. B., 13,* 5188-5192.
16. Monkhorst, H.J., & Pack, J.D. (1977). "Special points for Brillouin-zone integrations"—a reply. *Phys. Rev. B., 16,* 1748—1749.
17. Nørksov, J.K., Rossmeisl, J., Logadottir, A., Lindqvist, L., Kitchin, J.R., Bligaard, T., & Jónsson, H. (2004). Origin of the Overpotential for Oxygen Reduction at a Fuel-Cell Cathode. *J. Phys. Chem. B., 108,* 17886-17892.
18. Chua, C.K., Pumera, M., & Rulíšek, L. (2012). Reduction Pathways of 2,4,6-Trinitrotoluene: An Electrochemical and Theoretical Study. *J. Phys. Chem. C., 116,* 4243—4251.

ACADEMIC VITA

Brandon Perdue

bsp5195@psu.edu

Education

THE PENNSYLVANIA STATE UNIVERSITY — University Park, PA
Schreyer's Honors College — May 2022
Bachelor of Science in Chemical Engineering

AIGPE Lean Six Sigma Yellow Belt Certified — Deepwater, NJ, June 2021

Relevant Coursework

Process Fluid Mechanics	Chemical Reaction Engineering	Design of Chemical Plants
Process Heat Transfer	Chemical Process Safety	Chemical Engineering Laboratory
Mass Transfer Operations	Introduction to Polymers	

Professional Experience

THE CHEMOURS COMPANY — Deepwater, NJ
Manufacturing Technology Engineer — June 2020 – December 2020, June 2021 – August 2021
Constructed evaporator heating alternatives to optimize the simultaneous oil production of different product grades
Developed Krytox™ process algorithm to streamline contamination sources
Designed proper propagation arrestor per TFE Committee standards to prevent deflagration of TFE

THE PENNSYLVANIA STATE UNIVERSITY — University Park, PA
Instructional Assistant: Design of Chemical Plants — January 2021 – May 2021, January 2022 – Present
Counseled students with the principles of process design and economic evaluation in **food, pharmaceutical, and oil industries**
Managed online course materials through personal research and weekly instructor meetings
Advised 20+ teams in optimization of **Aspen processes** and **environmental impact modeling**
Concepts I assisted with: **Ammonia, biodiesel from waste cooking oil, and sustainable foods & beverages similar to DuPont Danisco®**

Leadership Experience

OMEGA CHI EPSILON: CHEMICAL ENGINEERING HONOR SOCIETY — University Park, PA
Penn State Chapter President — January 2021 – Present
Spearheaded the revival of the Penn State Chapter after two years of inactivity
Coordinated opportunities for chemical engineering students for professional development

CHEM E CAR: PENN STATE CHAPTER — University Park, PA
Chem E Car President — May 2020 – Present
Organized a diverse team of chemical engineers to collaboratively construct a model car run solely on chemical processes
Constructed a lab-made lead-acid battery and conducted research into upcoming battery tests for an all-iron redox flow battery

AICHE: PENN STATE CHAPTER — University Park, PA
Executive Board Member — May 2020 – Present
Organized events between professors, companies, and students to develop better foundations for chemical engineering curriculum
Constructed mentorship program with marketing and project manager at DuPont

BLUE & WHITE SOCIETY — University Park, PA
THON Morale Chair — August 2019 – Present
Planned, budgeted, and coordinated events to promote Penn State inclusion within the Penn State Alumni Association
Facilitated fundraising of $25,000+ for childhood cancer research

Activities & Honors

TAU BETA PI: ENGINEERING HONOR SOCIETY — University Park, PA
Member — January 2020 - Present
Advise engineering students towards academic excellence

Technical Skills

Aspen Plus complex system modeling
IP.21 inventory logging and data entry
SolidWorks advanced 3D modeling design
Advanced programming in Microsoft PowerBI, Microsoft Excel, and Minitab